Corrosion Science 232 (2024) 112049

Contents lists available at ScienceDirect

Corrosion Science

journal homepage: www.elsevier.com/locate/corsci

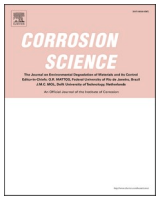

Improved corrosion and corrosion-wear properties of Fe-based high-entropy amorphous coatings by modulating heat input of HVAF

Yangzi Ye [a], Zhijun Guo [a], Zhenjie Zhou [a], Baosen Zhang [b], Qianqian Wang [a,b,*], Baolong Shen [a,**]

[a] School of Materials Science and Engineering, Jiangsu Key Laboratory for Advanced Metallic Materials, Southeast University, Nanjing 211189, China
[b] School of Materials Science and Engineering, Jiangsu Key Laboratory of Advanced Structural Materials and Application Technology, Nanjing Institute of Technology, Nanjing 211167, China

ARTICLE INFO

Keywords:
High-entropy amorphous coatings
Heat input
Corrosion resistance
Corrosion-Wear properties
HVAF

ABSTRACT

The $Fe_{34}Ni_{20}Cr_{20}Mo_5B_4C_4P_{12}Nb_1$ high-entropy amorphous coatings were fabricated via high-velocity air fuel (HVAF) with different heat input. The coating with the lowest heat input exhibits excellent corrosion resistance. The excessive heat input results in the formation of micro-oxidation zones, which reduces the corrosion resistance. The corrosion-wear behavior in 3.5 wt% NaCl solution has been investigated. Below the applied potential of Open-circuit Potential (OCP), the corrosion process is inhibited. Above the applied potential of OCP, a significant escalation in corrosion-wear synergy is observed with an increase in applied potential, particularly in terms of the volume loss attributed to the wear-induced corrosion.

1. Introduction

Fe-based bulk metallic glasses (BMGs) has attracted great research attention because of their excellent mechanical and chemical properties, such as high hardness, high strength, as well as excellent corrosion and wear resistance, which come from its distinctive long-range disordered structure and chemically homogeneous nature [1–3]. However, the industrial utilization of Fe-based metallic glass has been constrained by their inherent brittleness at ambient temperature, leading to a challenge in preparation and processing [4,5]. The fabrication of high-performance Fe-based amorphous coatings via thermal spraying has emerged as an effective strategy to expand the range of their industrial applications, of which high-velocity air fuel (HVAF) is a very promising method [6–8].

The corrosion and wear properties of the Fe-based amorphous coatings fabricated by thermal spraying techniques have been studied, including the effects of alloy composition, coating structure, and application environments [9–13]. The composition affects not only the corrosion resistance but also the glass-forming ability (GFA) of Fe-based alloy system. It was reported that Cr is a key element in the composition of passive films. The addition of Cr significantly improved the corrosion performance compared with the Cr-free Fe-based MGs because of the high passivation capability and the homogeneous structure of MGs, which allows the formation of homogeneous and stable passive films [9, 14–16]. The Fe-based MGs with more than 8 % Cr content showed spontaneous passive behavior, and for Cr content of ≥17 %, the passive films had excellent stability [17]. However, higher Cr contents leads to a decrease in the GFA of Fe-based MGs system [18]. The element Mo also improved corrosion and wear resistance, and small amounts of Mo can increased the GFA [19]. The addition of Mo prevented the Cr dissolution during the passivation process and enhanced the stability of the passive films. Nevertheless, the addition of excessive Mo caused electrochemical instability, attributed to the dissolution of Mo even at lower potentials and low stability of Mo-oxide compared to oxide/oxyhydroxide of Fe and Cr. Besides, the GFA decreased, and the cost increased with more Mo content [20,21]. Moreover, the partial replacement of Fe with Nb/Ni can improve the corrosion properties, and Nb is also effective in improving GFA [22–24]. The structure of the amorphous coatings is also crucial to its performance. The amorphous coatings fabricated by thermal spraying inevitably produce holes, oxides, crystalline phases, and other defects that are harmful to the localized corrosion properties of the coatings. Porosity is a major defect that affects the homogeneity of the coatings. Studies have shown that through-porosity can form diffusion paths that directly corrode the substrate. When the coating thickness is

* Corresponding author at: School of Materials Science and Engineering, Jiangsu Key Laboratory for Advanced Metallic Materials, Southeast University, Nanjing 211189, China.
** Corresponding author.
E-mail addresses: qwang678@seu.edu.cn (Q. Wang), blshen@seu.edu.cn (B. Shen).

https://doi.org/10.1016/j.corsci.2024.112049
Received 1 March 2024; Received in revised form 28 March 2024; Accepted 9 April 2024
Available online 13 April 2024

more than 240 μm, the through-porosity can be eliminated. Non-through porosity escalates the localized corrosion due to the decreased Cr/Fe ratios around the pores [25–28]. Corrosion resistance is more sensitive to amorphous content when porosity is below a certain level [29]. The Cr-depleted zones and crystal defects caused by oxides and crystalline phases are responsible for degradation in corrosion properties [30–32]. More seriously, these defects have a synergistic effect to accelerate corrosion. The defects and amorphous content of coatings is closely related to the preparation method and alloy system, such as the spraying parameters of HVAF, GFA of alloy systems. Furthermore, the service behavior of Fe-based amorphous coatings in environments (such as wear, erosion corrosion, hot corrosion, wet and dry cycling) and in corrosive media (such as H_3BO_3 solutions, NaCl solutions, HCl solutions, and so on) has been investigated [6,7,31,33–37]. However, the performance of the coatings at some critical synergistic environments such as stress corrosion, corrosion fatigue, and corrosion-wear hasn't been adequately investigated. In order to further promote the industrial application of Fe-based amorphous coatings, it is necessary to consider the effects of various usage environments, especially the corrosion-wear environment.

Optimizing the coating structure and corrosion performance by varying the heat input has been reported to be an effective strategy. It was found that with increasing power, the density, hardness, and wear resistance of the plasma sprayed Fe-based amorphous coatings increased, but the amorphous content decreased and the corrosion resistance increased and then decreased [11,38,39]. High spray rates and low spray temperatures result in higher density and amorphous content of HVAF Fe-based amorphous coatings [40]. However, the effect of heat input on the structure and corrosion performance of HVAF Fe-based amorphous coatings has been barely studied.

At 2003, the U.S. Navy developed the $Fe_{48}Cr_{15}Mo_{14}C_{15}B_6Y_2$ (SAM1651) and $Fe_{49.7}Cr_{18}Mn_{1.9}Mo_{7.4}W_{1.6}B_{15.2}C_{3.8}Si_{2.4}$ (SAM2×5) amorphous coatings and successfully put them into industrial application [41]. A lot of researches have been carried out on SAM1651 and SAM2×5 since then, including microstructure, defects, corrosion properties, wear properties, etc. Recently, researchers introduced "high--entropy" strategy to design amorphous alloys and prepared new materials called high-entropy amorphous alloys, which show significant improvement of corrosion performance, wear performance, and GFA, with promising potential in the field of amorphous alloy coatings [42–44]. Li et al. [44] developed a new $Fe_{20-35}Ni_{20}Cr_{20-30}Mo_{5-15}(P_{0.6}C_{0.2}B_{0.2})_{20}$ (configurational entropy ΔS_{conf}=1.67R-1.79 R) high-entropy BMGs with excellent thermal stability, good corrosion resistance, and low cost as a candidate for Fe-based amorphous coatings by means of a high-entropy alloy design strategy. The great thermal stability against crystallization and excellent corrosion resistance is attributed to the high mixing entropy and corrosion-resistant elements (Ni, Cr, Mo). Based on this system, our group designed and developed $Fe_{34}Ni_{20}Cr_{20}Mo_5B_4C_4P_{12}Nb_1$ (at %) (ΔS_{conf}=1.72 R) high-entropy BMGs with large GFA and excellent corrosion resistance by adding Nb element [45]. Besides, Fe-based amorphous coatings with excellent corrosion resistance and wear resistance were prepared by plasma spraying. However, there is still space to improve the performance of this coatings. In this work, Fe-based amorphous coatings with denser structure and higher amorphous content are prepared by HVAF. The structure and corrosion properties of Fe-based amorphous coatings with different heat input have been investigated. The corrosion-wear behavior of the coating has also been investigated to provide a reference for their application in corrosion-wear environments.

2. Materials and methods

2.1. Coatings preparation

$Fe_{34}Ni_{20}Cr_{20}Mo_5B_4C_4P_{12}Nb_1$ (at %) amorphous powders were synthesized by high-pure argon gas atomization using industrial-grade raw materials. The powders (less than 53 μm) were used as feedstock for preparing Fe-based amorphous coatings on 45 steel using high-velocity air fuel (HVAF) thermal spray system (Kermetico, USA). The samples were labeled as P1, P2, and P3, with the preparation parameters in Table 1. Basically, we control the heat input by varying the fuel pressure and air pressure, with P1 having the highest heat input and P3 having the lowest heat input. The substrate was cleaned with acetone, then thermal sandblasting two times and cold sandblasting once time before spraying. The materials used for sandblasting was 180 mesh white corundum.

2.2. Structure characterization

The phase of the powders and coatings was analyzed by X-ray diffraction (XRD, Bruker, D8 Advance) technique with Cu Ka radiation. The thermal stability of the samples was measured by differential scanning calorimetry (DSC, 404F3) at a heating rate of 0.67 K/s. The surface and cross-section morphology of the coatings were analyzed by scanning electron microscopy (SEM, Navo Nano SEM450), and the elemental distribution was analyzed by energy dispersive spectrometer (EDS). The porosity of the coatings was evaluated by quantitative image analysis performed on the SEM images using Image-Pro Plus 6.0 software. The nanostructure of the coatings was analyzed via transmission electron microscopy (TEM, Talos F200X). The chemical composition and oxidation state of passive films on the surface of coatings were analyzed using X-ray photoelectron spectroscopy (XPS, Thermo Scientific K-Alpha) with Al Kα excitation. The binding energies were calibrated using carbon contamination with C1s peak value of 284.8 eV. The standard binding energies of Fe 2p, Cr 2p, Ni 2p, Mo 3d, Nb 3d, C 1s, and O 1s were referred to the NIST XPS database. XPS ion beam sputtering with argon was used to analyze the depth profiles of the surfaces and the sputtering rate was 0.2 nm/s. The sputtering time was decided by a rule that the content of the main elements of the coatings was nearly constant. The XPS spectra were fitted and analyzed by AVANTAGE software.

2.3. Electrochemical measurements

The corrosion resistance measurements were carried out using the electrochemical workstation (Gamry interface 1000) in 3.5 wt% NaCl solution at room temperature. The electrochemical measurements were conducted in a three-electrode arrangement with a platinum counter electrode and an Ag/AgCl reference electrode. The samples were embedded in epoxy resin with an exposed area of 1 cm^2. All the coating samples were ground up to 2000 grits silicon carbide paper and then polished with 0.25 μm diamond paste before these tests. Potentiodynamic polarization curves were measured at a scanning rate of 0.5 mV/s after the samples were immersed for 30 min and the open-circuit potential became steady. Electrochemical impedance spectroscopy (EIS) measurements were performed at open-circuit potential and room temperature after a 30-minute exposure to the solution. The EIS of the samples was measured in the frequency range from 10^5 to 0.01 Hz with the perturbation amplitude of 10 mV. Fitting of the EIS data was performed using the Z_{view} software. The potentiostatic polarisation tests were conducted at 0.2 $V_{Ag/AgCl}$ to examine the stability of passive films.

Table 1
Spraying parameters employed in the HVAF process.

Parameter	P1	P2	P3
Spray distance (mm)	240	240	240
Air pressure (psi)	95	90	85
Fuel pressure (psi)	91	87	82
Hydrogen flow rate (SLPM)	35	35	35
Nitrogen flow rate (SLPM)	25	25	25
Powder delivery rate (rpm)	3	3	3
Traverse velocity (mm/s)	1000	1000	1000

All measurements were repeated at least three times to ensure good reproducibility. In order to analyze the chemical composition of the surface passive films of the P1, P2 and P3 coatings, the samples were analyzed using XPS after immersion in 3.5 wt% NaCl solution for 168 h. In order to analyze the thickness and composition of the passive films of the P3 coating at different polarization potentials, the samples used for XPS ion beam sputtering were polarized at 0 and 0.8 $V_{Ag/AgCl}$ in 3.5 wt% NaCl solution. The passive films for the Mott–Schottky analysis was obtained by immersing the material in 3.5 wt% NaCl solution for 1 h with a step of 10 mV/s at the frequency of 1 kHz.

2.4. Corrosion-wear measurements

The corrosion-wear properties of P3 coating and 304 SS were measured using a reciprocating ball-on-block tribometer (Rtec MFT-5000, USA) in 3.5 wt% NaCl solution and a three-electrode electrochemical workstation (Gamry interface 1000). The samples were ground up to 2000 grits silicon carbide paper and then polished with 0.25 μm diamond pastes before the corrosion-wear tests. The samples were immersed in 3.5 wt% NaCl solution for 30 min before the sliding wear test. The counterpart was a Si_3N_4 ball of 12.7 mm in diameter. The reciprocating distance was 3 mm. The applied normal contact load of the corrosion-wear tests was 30 N, the sliding speed was 30 mm/s with a stroke frequency of 5 Hz, and the test period was 30 min. The potentiodynamic polarization was measured from −0.75 $V_{Ag/AgCl}$ to 1.0 $V_{Ag/AgCl}$ with a scanning rate of 0.5 mV/s. The potentiostatic tests during sliding were conducted at constant potentials and the current transients were measured. After the corrosion-wear tests, the samples were ultrasonically cleaned with alcohol and then volume loss was measured using a 3D non-contact surface mapping analyzer (Bruker Counter GT K 3D). The worn tracks were characterized by SEM. The wear rates were calculated from the following equation [46]:

$$W = \frac{V}{D * L} \tag{1}$$

where W is the wear rate in mm^3/ (N m), V is the wear loss volume in mm^3, and D is the normal load in N, and L is the sliding distance in m.

In the corrosion-wear process, the volume loss of the sample is not only simple corrosion and friction loss but also loss generated by the corrosion-wear interaction. The following calculation formula can be used to evaluate the volume loss of each component [47–49].

$$V = V_W + V_C + \Delta V \tag{2}$$

where V is the total volume loss, V_W is the volume loss due to pure mechanical wear, which can be acquired by measuring the wear track at cathodic potential of −0.5 $V_{Ag/AgCl}$, V_C is the volume loss due to pure corrosion, and ΔV is the volume loss due to the synergistic effect of corrosion and wear. In general, the volume loss of the corrosion-wear synergistic effect consists of two components: the wear-accelerated corrosion volume V_{CW} and the corrosion-accelerated wear volume V_{WC}. Therefore, Eq. (2) can be rewritten as follows:

$$\Delta V = V_{CW} + V_{WC} \tag{3}$$

here, V, V_W can be obtained by the 3D non-contact surface mapping analysis, while V_C and V_{CW} can be calculated by Faraday's law with the following formula.

$$V_C = \frac{ItM}{nF\rho} \tag{4}$$

$$V_{CW} = \frac{I_r tM}{nF\rho} \tag{5}$$

where I is the current density before sliding and I_r the current density that increases during sliding, t is the sliding time (s), M is the atomic mass of the metal, n is the charge number participated in oxidation reaction, $n = 3$ was used due to the involved elements, F is the Faraday constant (C/mol), ρ is the density of the metal (g/cm^3). Finally, ΔV_W can be calculated by rearranging Eqs. (2) and (3).

3. Results and discussion

3.1. Phase and microstructure of coatings

Fig. 1(a) shows the XRD patterns of the feedstock powders and coatings. All of the patterns show a wide hump without any sharp diffraction peaks, indicating that the powders and coatings are amorphous. The formation of amorphous phase during gas atomization of the powders and the deposition of the coatings is attributed to the large GFA of the $Fe_{34}Ni_{20}Cr_{20}Mo_5B_4C_4P_{12}Nb_1$ (at %) alloy, as well as the large solidification rate of the preparation methods. Fig. 1(b) presents the DSC curves of the feedstock powders and coatings, all of which exhibit three exothermic peaks caused by crystallization. The crystallization temperature of the P1, P2, P3 coatings and the feedstock powders is 715 K, 720 K, and 726 K, 768 K respectively. The DSC curve of the ribbon is also measured, and the amorphous content of P1, P2, P3 coatings and feedstock powders can be calculated from the enthalpy of crystallization relative to that of the ribbon. The amorphous content of feedstock powders, P1, P2, and P3 coatings is 73 %, 61 %, 70 %, 82 %, respectively. The P3 coating has a much higher amorphous content than P1 and P2, even higher than the feedstock powders. "The amorphous content of the P3 coating is higher than that of the gas-atomized powder due to the high cooling rate of the HVAF spraying technique."

The splat morphology of the as-sprayed surfaces and the polished surfaces are shown in Fig. 2(a–f) and (g–i), respectively. The P1 coating, which is subjected to the maximum heat input, exhibits a rough and uneven surface with numerous large cell-like features; the P2 coating displays similar surface protrusions but the cell-like features are less in amount and smaller in size; P3 coating, receiving the minimum heat input, demonstrates superior surface smoothness without any noticeable cell-like structure. Further observation from the corresponding magnified images of P1 and P2 coatings (Fig. 2d-e) reveals that cell-like structure surfaces comprise unfused and inadequately spread particles, with a diameter of less than 10 μm. As indicated by Fig. 2(f), oxygen content at point A within the flat spread region is 20 %, which is lower than that at point B of the unfused powders (64 %). The above results infer that excessive heat input leads to oxidation in smaller powder particles, which prevents them from fusion and spreading. These unfused particles agglomerate into cell-like structure and form a rough surface. The backscattered SEM images of the polished top surfaces of P1, P2, and P3 coatings are shown in Fig. 2(g-i), respectively. The annular micro-oxide zones are found in the P1 and P2 coatings, corresponding to the cell-like structures observed in the unpolished surfaces. In contrast, the P3 coating exhibits a dense structure with few pores and no visible oxidation zone.

Fig. 3 shows the cross-section morphology of the P1, P2, and P3 coatings. All the three coatings, with a thickness ranging from 400 to 500 μm, exhibit strong adhesion to the substrate. The black substance at the interface between the coating and substrate is the residual Al_2O_3 from sandblasting. The primary defects within the P1 and P2 coatings are micro-oxide zones and pores. The cross-sections of the micro-oxide zones show a fan-like appearance. The P3 coating exhibits a superior cross-section quality devoid of visible large pores or micro-oxide zones. A declining trend in coating porosity is observed from P1 to P3, with the porosity volume percentages being 0.82 %, 0.73 %, and 0.17 % for P1, P2, and P3 respectively.

The micro-oxide zone of the P2 coating was analyzed by TEM and EDS, as shown in Fig. 4. In this area, a lot of spherical particles (tens of nanometers to a few micrometers) coming from the unfused feeding powders are found, and these particles lead to the formation of porous structure, as shown in Fig. 4(a). Closer observation in Fig. 4(b-c) shows that these particles have good sphericity and a core-shell structure with

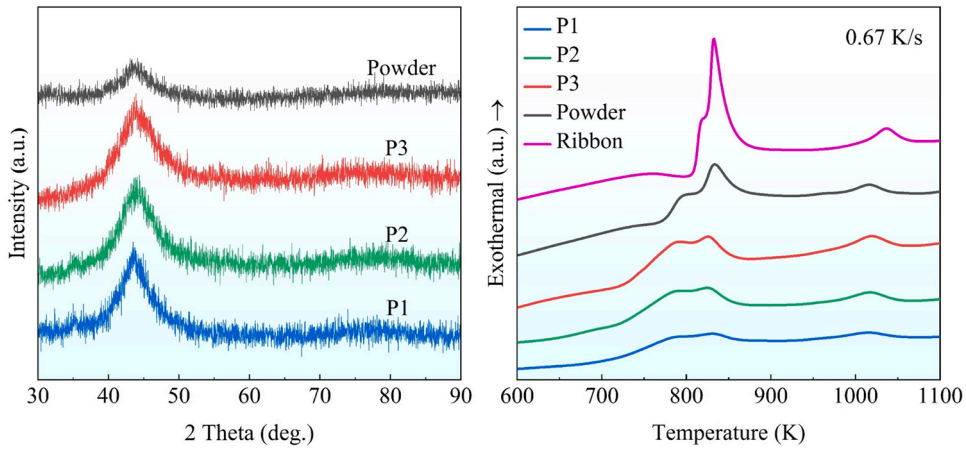

Fig. 1. (a) XRD patterns and (b) DSC curves of the powder and P1, P2, P3 coatings, the DSC curve of the ribbon is shown for comparison.

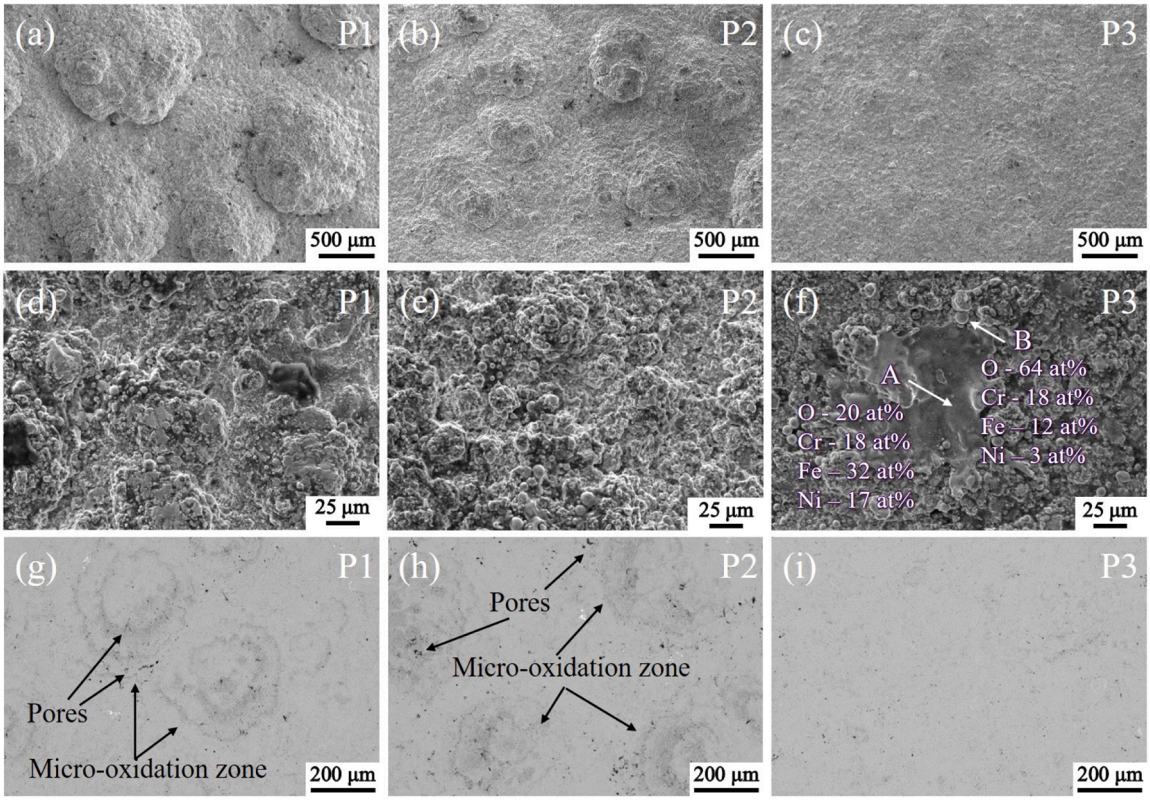

Fig. 2. SEM micrographs of (a–c) the as-sprayed P1, P2 and P3 coatings and (d–f) the corresponding enlarged images; (g-i) the polished top surface of the P1, P2 and P3 coatings.

a shell thickness of about tens of nanometers. The EDS analysis shows that the outer layer is oxidized and enriched with Cr, Nb, and O elements, while the inner layer maintains the composition of the original powder. It can be inferred that the powders with a smaller particle size have a larger specific surface area, which is easier to oxidize during the spraying process. Due to the relatively low temperature and fast spraying speed of HVAF technology, only the outer layer of powders was oxidized. The oxidized powder is difficult to spread and tends to aggregate to produce micro-oxide zones with a porous structure. The micro-oxide zone shows a porous structure due to the fact that the oxidized powder cannot spread and the powders do not bond well with each other. The high-resolution TEM image of the core-shell structure of the powder is shown in Fig. 4(d), with the FFT pattern shown in the inset. Lattice fringe is observed in the shell (as noted by the yellow dashed lines), indicating the oxidized shell is crystalline. The FFT pattern of the shell confirms it is the $FeCr_2O_4$ phase. No lattice fringe is observed for the core, revealing its amorphous nature. This micro-oxide zone is prone to pitting corrosion. Besides, the oxides and the pores can couple with each other to accelerate the corrosion, which is the main factor affecting the corrosion performance of the P2 coating. Fig. 4(e) shows the EDS line results for the distribution of the key elements along the yellow arrow in Fig. 4(b). The oxide layer is mainly enriched with Cr and O elements in similar proportions, while the Fe and Ni elements have higher concentration in the core. In the core region, the content of Cr elements is significantly lower compared to the nominal composition, due to the enrichment of Cr in the oxide layer. The amount of Mo and Nb

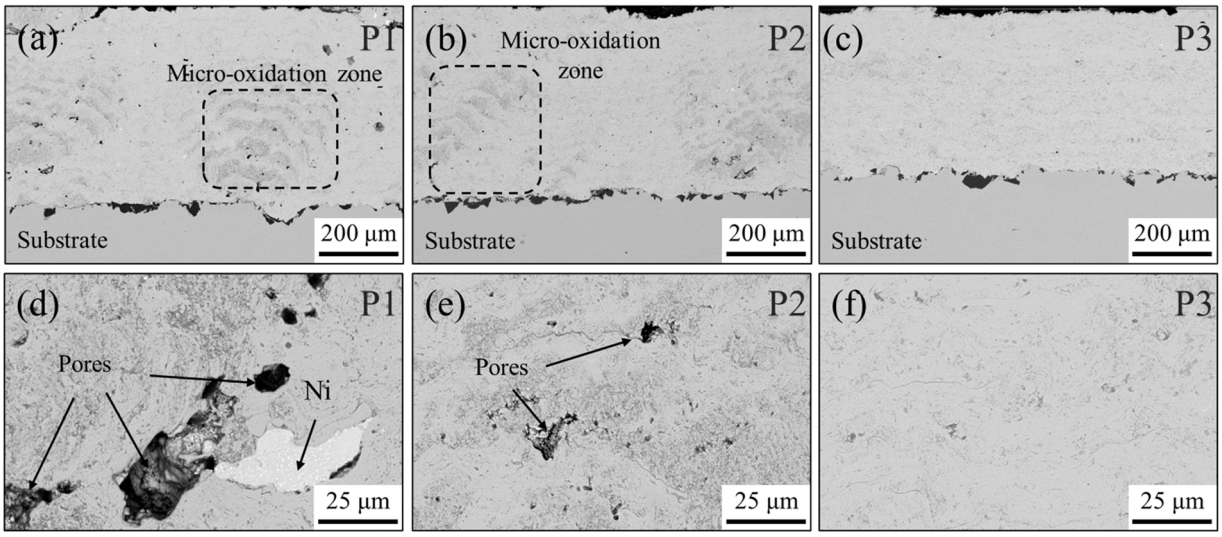

Fig. 3. Back-scattered SEM micrographs of (a–c) the cross-section surface and (d–f) the enlarged images of the P1, P2 and P3 coatings.

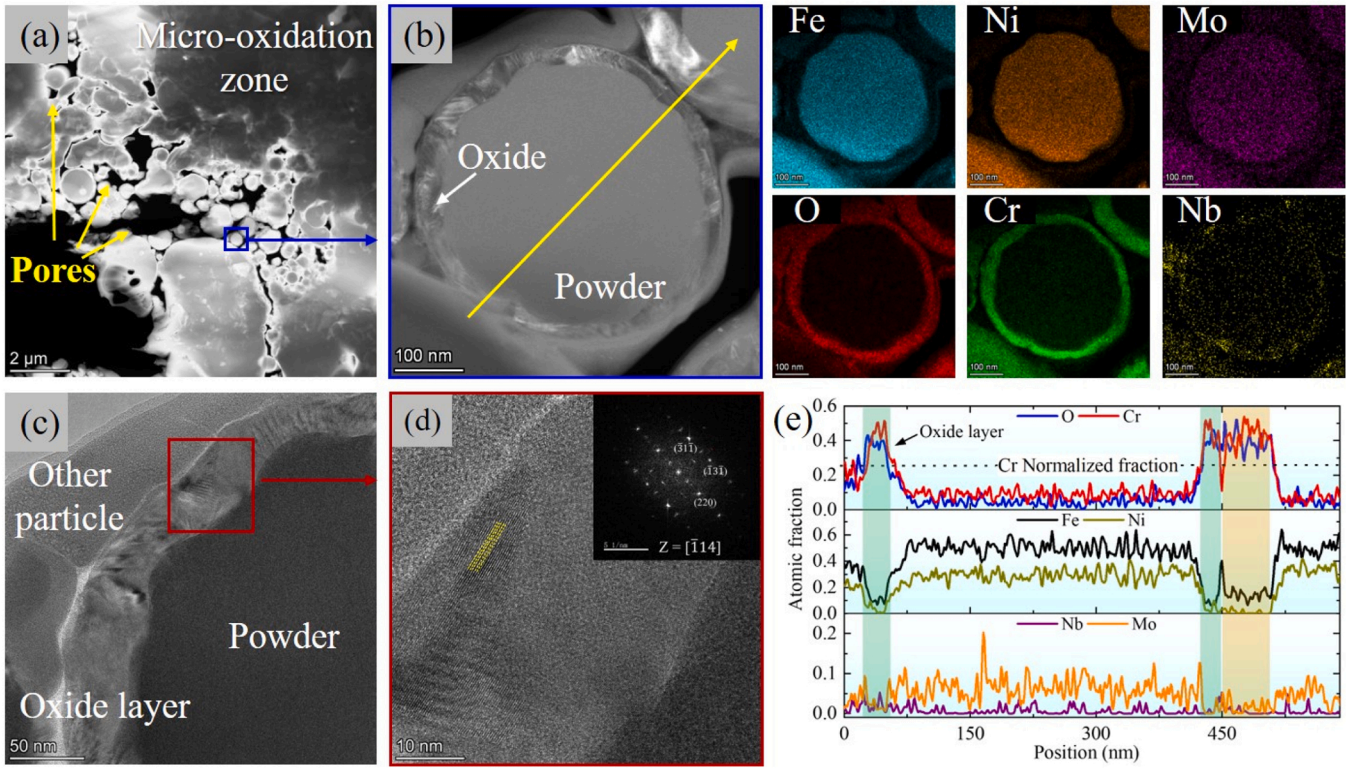

Fig. 4. (a) Dark-field (DF) TEM image of the micro-oxidation zone of P2 coating; (b) DF image and the element distribution of individual powder of the micro-oxidation zone; (c, d) the HRTEM images of the oxide layer, the inset is the FFT of (d) ; (e) EDS line scan along the yellow arrow in (b).

elements are very small and do not change significantly.

Fig. 5 shows the typical nanostructure of P3 coating analyzed by TEM and EDS. The presence of many round oxide particles of tens of nanometers in the amorphous matrix is shown in Fig. 5(a). The featureless atoms arrangement and the diffuse halo ring of the SAED pattern shown in Fig. 5(b) indicate a complete amorphous phase for the matrix. The smaller-sized oxides predominantly exhibit an amorphous state as shown in Fig. 5(c). Another kind of the oxide is observed in P3 coating, with the nanostructure shown in Fig. 5(d), consisting of different small grains, which is believed to be the initial stage of crystallization. Its element distribution is shown in Fig. 5(g), which is mainly enriched in Cr and O. No obvious element segregation is observed inside the particle, indicating the small grains in the particle has similar composition. Fig. 5 (e-h) shows the morphology and elemental distribution of the large-size oxides in the P3 coatings, which are also rich in Cr and O elements. The HRTEM and SAED patterns in Fig. 5(f) indicate the crystalline oxide is $FeCr_2O_4$ phase. No micro-oxide region is observed in the P3 coating. The above analysis suggests a gradual crystallization process of the oxides can be observed in the P3 coating, i) the amorphous oxide start to form in the amorphous matrix due to the affinity of Cr and O, ii) due to the temperature increase during spraying, small grains nucleate in the amorphous oxide, iii) and then grow into large ones.

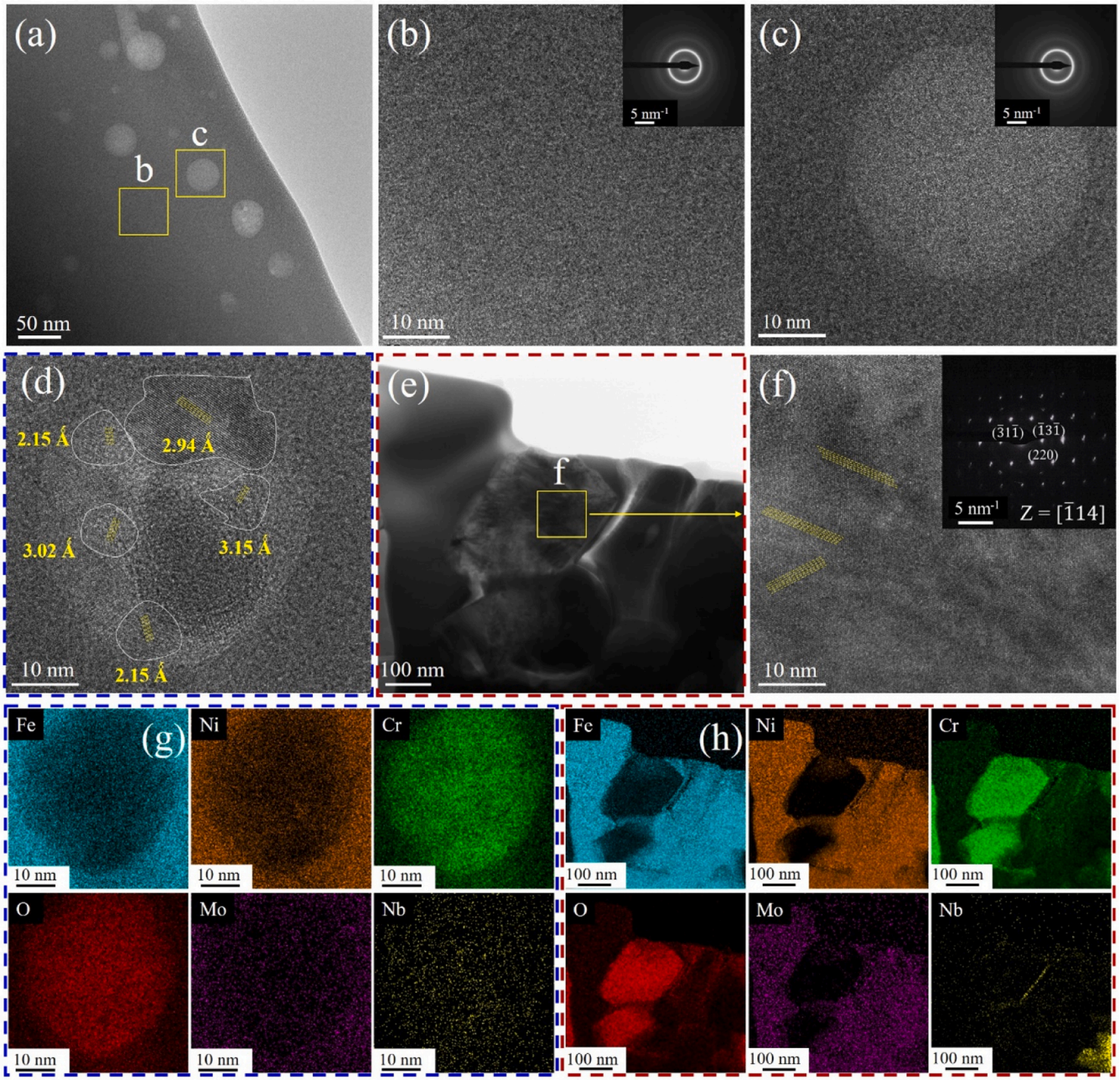

Fig. 5. Bright-field (BF) images of (a) P3 coating; HRTEM images of (b) the amorphous matrix, (c) the small-size amorphous oxide, and (d) the crystalline oxide; (e) BF image, (f) HRTEM image (with the SAED pattern in the inset) of large-size crystalline oxide; (g, h) EDS mapping results of (d, e).

3.2. Corrosion behavior of the coatings and passive films stability

The corrosion performance of the coatings is analyzed and compared with the reported materials. Fig. 6(a) shows the potentiodynamic polarization curves of amorphous coatings, 45 steel, 304 SS, and the $Fe_{34}Ni_{20}Cr_{20}Mo_5B_4C_4P_{12}Nb_1$ (at %) coating prepared using the Atmospheric Plasma Spraying (APS) method [45] in a 3.5 wt% NaCl solution, with the results listed in Table 2. As the heat input of the HVAF coatings decreases, the E_{corr} increases gradually while the I_{corr} and I_{pass} decrease steadily. The P3 coating exhibits superior corrosion performance, with the noblest E_{corr} of −238 mV, the lowest I_{corr} of 8.0×10^{-7} A/cm^2, and the lowest I_{pass} of 1.2×10^{-6} A/cm^2, respectively. All the HVAF coatings exhibit higher corrosion potential and lower corrosion current density than 45 steel, 304 SS and APS coating, indicating the advantages of the HVAF method. The corrosion potential and corrosion current density of P3 coating are compared with other Fe-based HVAF/HVOF amorphous coatings that have been reported, as shown in Fig. 6(b) [6,31,50–57]. The P3 coating has lower corrosion current density and higher corrosion potential than the reported coatings, indicating its excellent corrosion resistance in the 3.5 wt% NaCl solution. Although the HVAF $Fe_{52}Cr_{26}Mo_{17}C_{2.5}B_{2.1}Si_{0.4}$ amorphous coating exhibits the same corrosion current density and higher corrosion potential, it has higher Cr and Mo content, resulting in higher costs.

In order to evaluate the electrochemical reactions at the coatings surface, EIS measurements were conducted. The Nyquist plots, Bode impedance plots, and Bode phase angle plots of P1, P2, and P3 coatings are shown in Fig. 7(a–c), respectively. From the Nyquist plot in Fig. 7(a), it can be seen that the capacitive arc diameter of the Nyquist plots for P3 coatings is much larger than that of the P1 and P2 coatings, which indicates the superior corrosion resistance of the P3 coating [39]. The

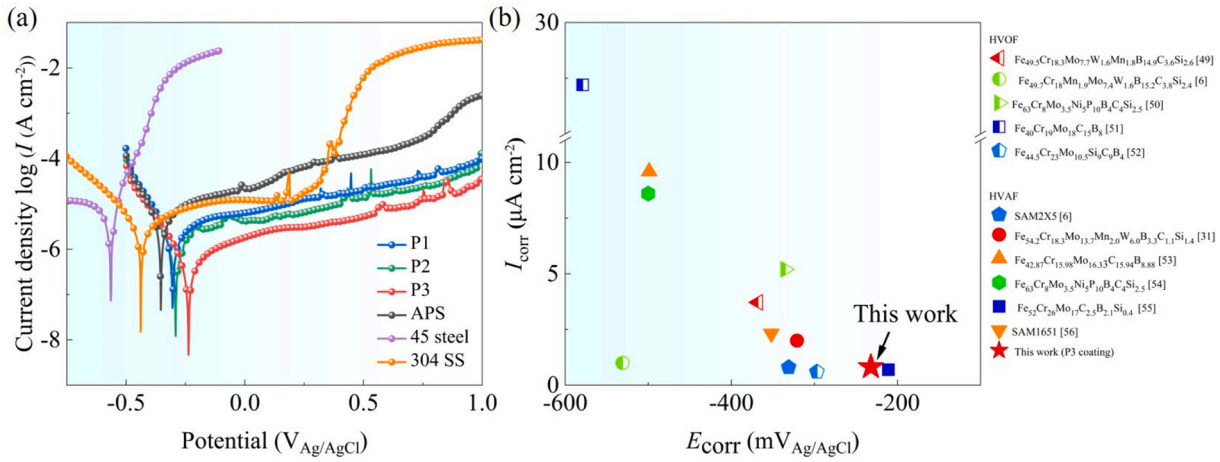

Fig. 6. (a) Potentiodynamic polarization curves of the P1, P2 and P3 coatings, APS coating, 405 steel and 304 SS in 3.5 wt% NaCl; (b) comparison of the corrosion potentials and corrosion current densities in 3.5 wt% NaCl solution of the reported Fe-based amorphous coatings prepared by HVAF/HVOF methods.

Table 2
Electrochemical parameters obtained from potentiodynamic polarization tests.

Samples	P1	P2	P3	APS	45 steel	304 SS
E_{corr} (mV)	-292	-278	-238	-335	-566	-438
I_{corr} (μA cm^{-2})	3.1	1	0.8	5.1	14.8	5.3
$I_{pass(0.2\ V)}$ (μA cm^{-2})	6.1	4.2	1.2	3.1	-	4.9

high-frequency capacitive loops arise due to passive film resistance on coating while low-frequency loops are attributed to charge transfer resistance during the electrochemical reaction process. A linear region discerned in P1 and P2 coatings relates to Warburg impedance (Z_W), which appears due to the diffusion channels leading to internal corrosion [58]. The presence of a large number of Cr-rich oxide particles and pores in the micro-oxidized zone leads to more Cr-poor zones and heterogeneous phases, which are susceptible to corrosion. As corrosion proceeds, the Cr-poor zone dissolves and oxide particles may be dislodged, forming channels for ion (Cl^-, H^+, $M^{\delta+}$) diffusion. Besides, the "plugging effect" caused by local accumulation of corroded products in the coating defects restricts the ion mass transfer between the active zones and aggressive solution and consequently leads to the Warburg impedance behavior [6,32,59–61]. Some of the reactions that occur during corrosion are listed below [35,62] :

$$m \rightarrow M^{\delta+} + \delta e^- \quad (6)$$

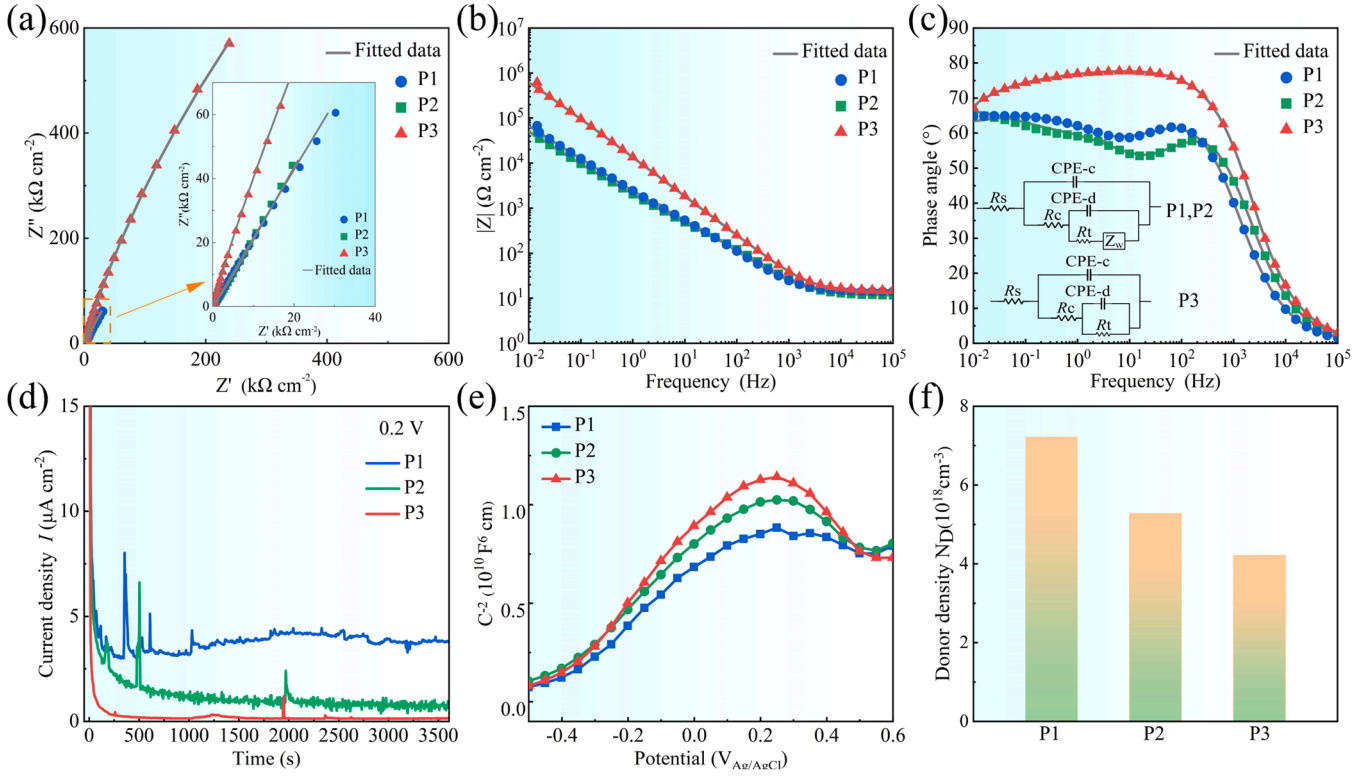

Fig. 7. (a) Nyquist plots, (b) Bode impedance, (c) Bode phase angle plots (the insets are equivalent circuit models) of the P1, P2 and P3 coatings; (d) Potentiostatic polarization plots, (e) Mott-Schottky plots, (f) donor concentration of the P1, P2 and P3 coatings.

$$m + \frac{\chi}{2} H_2O \rightarrow MO_{\frac{\chi}{2}} + \chi H^+ + \chi e \quad (7)$$

$$MO_{\frac{\chi}{2}} + \chi H^+ \rightarrow M^{\chi+} + \frac{\chi}{2} H_2O \quad (8)$$

where, the m represents the dominating metallic components of the coating (Fe, Cr, Ni or Mo).

Corrosion behavior of the coatings can also be uncovered from Bode plots as shown in Fig. 7(b and c). The Bode impedance plots reveal that all the coatings demonstrate resistive behavior towards high frequencies, while displaying capacitive behavior within intermediate and low frequencies. The maximum phase angle for the P1, P2 and P3 coatings are 65.3°, 64.8° and 77.6°, respectively. Moreover, the P3 coating exhibits the highest impedance value, indicating its superior barrier property and enhanced capacitive behavior of double layer among all the coatings [63]. The Bode angle phase plots are shown in Fig. 7(c) with the insets showing the equivalent circuit model (EEC) for P1, P2, and P3 coatings. The R_s is the solution resistance; R_c is the coating resistance; CPE (constant phase element) represents the dielectric properties of the coating; CPE-c is the non-ideal capacitance of corrosion product films; CPE-d is the double layer capacitance between the solution and coating/substrate within the defects. Considering the ideality of the equivalent circuit system, the capacitors in the circuit are replaced by CPE. The calculation method is shown in Eq. (9) [64].

$$Z_{CPE} = \frac{1}{f_0(j \times w)^n} \quad (9)$$

where j is an imaginary number, w is the angular frequency and f_0 is a proportionality coefficient. n is the frequency factor, when $0 < n < 1$, CPE represents the distribution of dielectric relaxation time in frequency space. R_t is charge-transfer resistance during corrosion reaction; Z_W employed for P1 and P2 coatings is diffusion resistance of corrosive species through pores or micro-oxide zones. The n values are derived from the fitting results, and the values are from 0.85 to 0.61, indicating the presence of constant phase elements in the circuit instead of pure capacitance.

The results of EIS fitting for P1, P2 and P3 coatings are presented in Table 3. Chi-square $\chi 2$ is the parameter to asses system error. The $\chi 2$ of the coatings is within the range from 2×10^{-4} to 2.5×10^{-4}, which demonstrates that the equivalent circuit is rational and the fitting results are reliable. The variation of R_s is very small and therefore has a negligible effect on the corrosion process. The P3 coating has a relatively low value of CPE-c and a relatively high value of R_c, which suggests that it has a better corrosion resistance among the three coatings [32,61,65]. The impedance values in the low frequency range in the Bode impedance diagram (Fig. 7b) are related to the R_t during corrosion at the coating/electrolyte interface. A higher value of impedance amplitude indicates a higher R_t, which is related to the higher corrosion resistance of the coating when exposed to aggressive solutions (NaCl solution). Among the three coatings, the P3 coating has the highest R_t, further confirming its excellent corrosion resistance in saline environment. The lower R_t values of P1 and P2 coatings come from the increased reaction rate between the ions and the coating [6,32,61,62], which is due to the presence of the pore/micro-oxide zones.

The average passive films thickness can be calculated from the capacitance value CPE in EEC. The relationship between the capacitance and passive film thickness d is as follow [66]:

$$d = \frac{\varepsilon \varepsilon_0 A}{C} \quad (10)$$

Where ε is the dielectric constant of the passive film (15.6 for Fe-Cr alloy), ε_0 is the vacuum permittivity (8.854×10^{-14} F cm^{-1}), A is the effective tested area (1 cm^2 in this work). However, the physical interpretation of CPE in EEC is still ambiguous and the passive film capacity C cannot be simply replaced by the fitted value of CPE-T. Thus, some scholars proposed assumptions and models to extract the effective capacitance Q_{eff} [67] to evaluate the passive film properties. Considering that oxide film thickness formed on the amorphous coating surface are several nanometers, the power-law model put forward by Hirschorn [68,69] was utilized in this study. The hypothesis in power-law includes that the time constant distribution is normal to the electrode surface. Correspondingly, Q_{eff} is expressed as:

$$Q_{eff} = gQ(\rho_\delta \varepsilon \varepsilon_0)^{1-n} \quad (11)$$

The relationship between g and n as follows: $g = 1 + 2.88(1 - n)^{2.375}$, where n derives from the fitting value in the equivalent circuit, as shown in Table 3; ρ_δ is the resistivity and its upper bound is applied from the following equation Eq. (12):

$$\rho_{\delta,max} = \frac{1}{2\pi f_{max} \varepsilon \varepsilon_0} \quad (12)$$

Where f_{max} is the highest frequency during the EIS measurement (10^5 Hz). Finally, the average thickness of passive film is calculated as Eq. (13):

$$d = \frac{\varepsilon \varepsilon_0 A}{Q_{eff}} \quad (13)$$

Based on the above formula, the passive film thickness of P1, P2, and P3 coatings are 4.15, 3.45, and 6.65 nm, respectively. The P3 coating has the thickest passive film due to its dense structure, contributing to the most excellent corrosion resistance.

The passive films stability of the P1, P2, and P3 coatings is analyzed under potentiostatic at a potential of 200 $mV_{Ag/AgCl}$, with the potentiostatic polarization curves shown in Fig. 7(d). In the initial stages of polarization, the current densities of all the coatings exhibit a rapid decline before gradually stabilizing due to the formation of passive films [70–72]. The P3 coating demonstrates lower current density compared to P1 and P2 coatings, which is consistent with the potentiodynamic polarization results. The current densities of P1 and P2 coatings exhibit pronounced fluctuations in response to the alternating growth and destruction of passive films, suggesting the inhomogeneity during the passive films growth, which is potentially linked to the surface pores and micro-oxide zones [28,73]. In contrast, the current density of P3 coating almost nearly constant, signifying an equilibrium between the passive film growth and dissolution. The above analysis shows that P3 coating possesses more homogeneous passive films than the P1 and P2 coatings.

The Mott-Schottky plots of the passive films of the three coatings at 0.4 $V_{Ag/AgCl}$ are shown in Fig. 7(e). A linear region with a positive slope at − 0.5–0.2 $V_{Ag/AgCl}$ and a linear region with a negative slope at 0.2–0.6 $V_{Ag/AgCl}$ are observed for all the three coatings. The bilayer structure of the passive films in Fe-Cr-Ni based alloys results in the change from n-type to p-type semiconducting [74]. Both donor concentration N_D and the acceptor concentration N_A can reflect the defect density in the passive films, here we only calculating N_D for evaluation. The straight lines with positive and negative slopes reveal the n-type and p-type semiconducting characteristic of the passive films, respectively. The donor concentration (N_D) can be calculated by the space charge capacitance using the following equations [75]:

Table 3
Values of fitting parameters obtained from EIS spectra.

Samples	P1	P2	P3
R_s (Ω cm^2)	11.59	13.92	14.87
CPEc- T (μF cm^{-2}s^{n-1})	39.83	47.85	10.92
CPEc-n	0.81	0.81	0.85
R_c (Ω cm^2)	452	961	63,147
CPEd-T (μF cm^{-2}s^{n-1})	79.73	66.04	1.76
CPEd-n	0.71	0.68	0.61
R_t (Ω cm^2)	30,988	65,976	461,060
Z_w- R_w (Ω cm^2)	46,251	45,021	-
Z_w-τ	2.063	1.037	-
Z_w-p	0.38	0.59	-
$\chi 2(10^{-4})$	2.1	2.1	2.4

$$\frac{1}{C_{SC}^2} = \pm\frac{2}{\varepsilon_r\varepsilon_0 q N_D}(E - E_{fb} - \frac{kT}{q}) \quad (14)$$

Where ε_r is the dielectric constant of the passive films (15.6 for Fe-Cr alloy), ε_0 is the vacuum permittivity (8.854×10^{-14} F·cm^{-1}), q is the elementary charge (1.602×10^{-19} C), E_{fb} is the flat band potential, k is the Boltzmann constant (1.38×10^{-23} J·K^{-1}), and T is the absolute temperature. The value of kT/q can be neglected because it is only ~25 mV at room temperature. The N_D of the P1, P2, and P3 coatings are 7.22×10^{18}, $5.28 \times 10^{18,}$ and 4.21×10^{18} cm^{-3}, respectively, as shown in Fig. 7(f). A higher N_D indicates that there are more defects in the passive films, and the Cl^- in the solution can easily penetrate the coatings; whereas a lower N_D indicates that the passive layer is denser, with fewer defects, and better corrosion resistance [76,77]. Since there are no chemical variations in the P1, P2, and P3 coatings, the difference in the passive films arises from the microstructure of the coatings. Therefore, it can be deduced that the better corrosion resistance of P3 coating is attributed to fewer defects and denser passive films.

Fig. 8 shows the surface morphologies of P1, P2, and P3 coatings after 1 h potentiostatic polarization at 0.2 $V_{Ag/AgCl}$. The P1 coating exhibits numerous continuous corrosion zones surrounding the micro-oxide zones and pores, and the P2 coating displays extensive pitting along with some continuous corrosion zones. In contrast, only a small amount of corrosion pits is observed in the P3 coating. The corresponding enlarged images reveal that among all the coatings, P1 has the deepest corrosion pits, followed by P2, while P3 has the shallowest corrosion pits. The oxides and pores are formed during the spraying process, leading to localized Cr depletion, thereby deteriorating corrosion resistance of the coatings, as these defects can influence the formation of the passive films and even instigate internal corrosion of attached ions [28]. This aligns with the previous analyses. Owing to numerous micro-oxide zones and pores, P1 and P2 coatings demonstrate poor resistance to corrosion and pitting. Conversely, superior corrosion and pitting resistance exhibited by P3 can be attributed to its dense coating structure coupled with minimal defects.

The XPS analysis was utilized to examine the chemical states of the metallic elements in the passive films of the P2 and P3 coatings. Here we focus only on the metallic elements associated with corrosion, as the metallic elements are more important for the formation of oxidation films. For both the P2 and P3 coatings, Fe, Ni, Cr, Mo, and Nb are detected in both oxidized and metallic states. There is no significant difference in the elemental valence and constitution of the passive films of the two coatings. The relative contents of Fe, Ni, Cr, Mo, and Nb elements detected by XPS can be calculated using the areas of peaks and the relative sensitivity factors of elements. The results are summarized in Fig. 9(f). Compared to the nominal composition, the passive films are more abundant in Fe, Cr, Mo, and Nb, but a lower amount in Ni. Elements such as Fe, Mo, Cr, and Nb have a stronger chemical affinity for oxygen than Ni does, making them more prone to oxidation [44]. Cr is a key passivation element that contributes to the high corrosion resistance, while Mo stabilizes the passive films by preventing Cr dissolution during the passive process and enriching the passive films with Cr [19–21]. The passive films of P3 coating have a higher content of Cr and Mo. As a result, the passive films of P3 coating have a more stable and dense structure that inhibits further dissolution. This is also integral to its excellent coating structure and high corrosion resistance of the alloy system.

To further analyze the passive films of the P3 coating, the XPS etching analysis was performed after the P3 coating is polarized at 0 and 0.8 $V_{Ag/AgCl}$, respectively. The variation of the composition with the sputtering time for the above two samples is shown in Fig. 10 (a-b), respectively. The thickness of the passive films is determined as the sputtering time at which the oxygen content is halved relative to the surface, as shown in the black dashed line in Fig. 10(a-b). For the samples etched at 0 and 0.8 $V_{Ag/AgCl}$, the time required to etch half of the passive films increases slightly (from 24.9 to 25.4 s), indicating that the thickness of the passive films remains essentially stable at 0–0.8 $V_{Ag/AgCl}$. Fig. 10(c-d) present the normalized concentrations of the metallic elements in the passive films at 0 and 0.8 $V_{Ag/AgCl}$, respectively. As the sputtering time increases, the percentages of metallic states increase while those of oxidized states decrease. Passive films are composed of oxides and hydroxides with various metals. Cr is the primary element constituting the passive films and exists as Cr_{ox}^{3+} and Cr_{hy}^{3+}. As the potential rises from 0 to 0.8 $V_{Ag/AgCl}$, the percentage of oxidized state of the metal element increases from 80 % to 90 %, corresponding to an increase in the passive films thickness. A high content of oxidized state, particularly Cr, Ni, Mo, and Nb elements that are known for excellent corrosion resistance, endows the passive films with superior protective performance. Through the above analysis, P3 coating shows excellent corrosion resistance and strong passivation capability, which is correlated with its dense coating structure, high amorphous content and the excellent performance of the high entropy system itself.

3.3. Corrosion-Wear behavior of the P3 coating

Based on the above results, the P3 coating with the lowest heat input exhibits the best corrosion performance. Thus, the corrosion-wear behavior of the P3 coating is analyzed and compared with 304 SS. Fig. 11(a) shows the OCP variation curves of the P3 coating and 304 SS

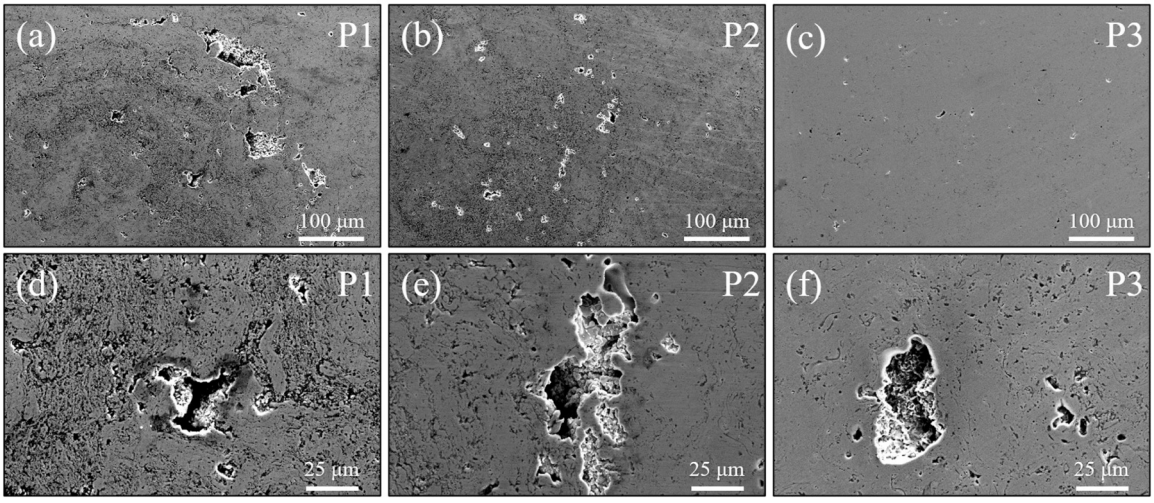

Fig. 8. Surface morphology of (a) P1, (b) P2, (c) P3 coatings after 1 h potentiostatic polarization; (d-f) the corresponding enlarged images.

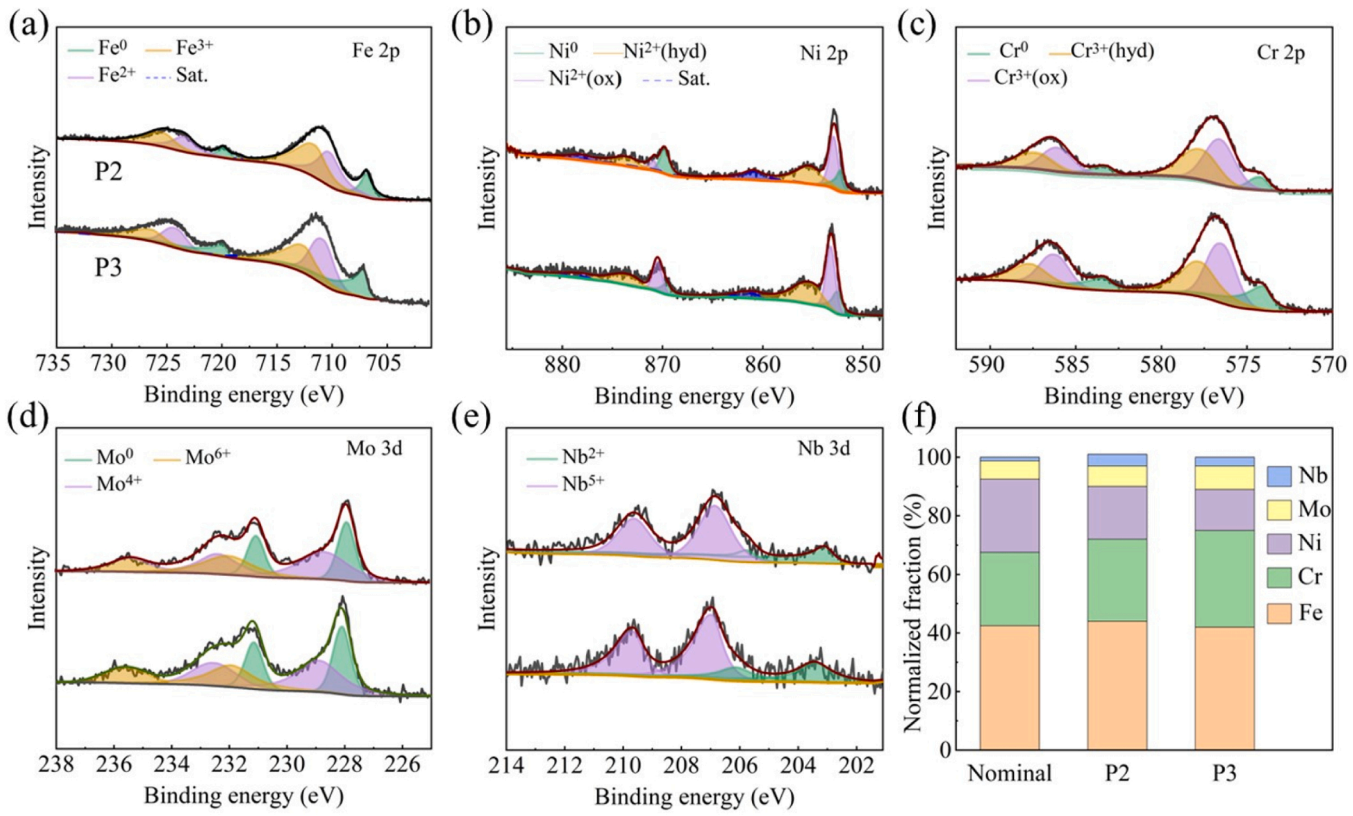

Fig. 9. XPS spectra of (a) Fe 2p, (b) Ni 2p, (c) Cr 2p, (d) Mo 3d and (e) Nb 3d detected for passive films on the P2 and P3 coatings after immersing in 3.5 wt% NaCl solution for 168 h; (f) the relative contents of Fe, Cr, Ni, Nb and Mo elements on the surface.

under corrosion-wear condition in the 3.5 wt% NaCl solution. At the start of the sliding, the OCP of P3 coating and 304 SS drops sharply due to the damage or removal of surface passive films. The OCP measured during sliding is a mixture of potentials of the loaded and unloaded surfaces. This is because a galvanic coupling is formed between the passive surface (unloaded surface) and the passive-damaged surface (loaded surface). Damage to the passive films may increase the anodic reaction and cathodically polarize the surrounding surfaces, leading to the cathodic shift of OCP [78–80]. During the sliding process (600–2400 s), the OCP value of the P3 coating is always higher than that of 304 SS, and the fluctuation is smoother, which indicates that the P3 coating has more excellent corrosion resistance. After sliding, the OCP starts to increase suddenly (anode movement) due to the repassivation of the worn surface. Fig. 11(b) is the friction coefficient of the P3 coating and 304 SS under the OCP test. The difference in the friction coefficient between the P3 coating and 304 SS is not significant, both within the range of 0.55–0.6.

Fig. 11(c) shows potentiodynamic polarization curves of P3 coating and 304 SS under sliding in 3.5 wt% NaCl solution, with the results summerized in Table 4. The corrosion potential and corrosion current density are −404 mV and 34 μA/cm^2 for P3 coating, and −417 mV and 44 μA/cm^2 for 304 SS respectively. During the polarization process, the passive current density of P3 coating is consistently smaller than that of 304 SS, indicating that P3 still has superior corrosion resistance to 304 SS under corrosion-wear conditions. For both the P3 coating and 304 SS, a decrease in the E_{corr} and an increase in the I_{corr} and I_{pass} is found compared to the corrosion process without loading, indicating the deterioration of corrosion resistance due to wear.

Fig. 11(d) is the friction coefficient of the P3 coating and 304 SS under the potentiodynamic polarization test. Initially, in the cathodic polarisation stage, it is considered that there are no corrosion products and the friction coefficient is large. As the corrosion proceeds to the anodic polarisation stage, the friction coefficient suddenly decreases due to the lubrication effect of the formed passive films. The friction coefficient of the P3 coating changes approximately 150 seconds later than that of 304 SS, which indicates that the P3 coating has a higher corrosion potential, and thus better corrosion resistance.

The wear rate and wear volume of P3 coating and 304 SS under corrosion-wear condition are shown in Fig. 11(e). The wear volume and wear rate for P3 coating are 0.93×10^{-3} mm^3 and 1×10^{-6} mm^{3}N^{-1}m^{-1}, while for 304 SS are 2.96×10^{-3} mm^3 and 3.2×10^{-6} mm^{3}N^{-1}m^{-1}, respectively. Both the wear rate and the wear volume of the P3 coating are one-third of that of 304 SS. Fig. 11(f) presents the typical surface profiles measured across the wear tracks. The dimensions of the 304 SS profile are larger than those of P3. It is worth noting that the ridges, i.e., material buildup, occur at all wear edges due to the large plastic deformations produced during corrosion-wear. From the above analysis, it can be concluded that the P3 coating has better corrosion-wear resistance than 304 SS.

The surface morphology of 304 SS and the P3 coating after the corrosion-wear test is analyzed. As shown in Fig. 12(a). The width of the worn area of 304 SS is 1 mm and the length is 3 mm. A large number of elongated furrows can be seen on the surface as well as a dark films in the middle. Fig. 12(b) is an enlarged picture of the dark area in the middle of the Fig. 12(a). The films are not completely destroyed, although there are many cracks in the middle, due to the periodic applied loads. Fig. 12(c) shows the morphology of the heavy furrows of Fig. 12(a), exhibiting a typical abrasive wear mechanism. As shown in Fig. 12(d), similar to 304 SS, the wear morphology of P3 is also composed of a large number of furrows and some incompletely disrupted films but the furrows of P3 are much shallower, which indicates a weaker degree of abrasive wear. As shown in Fig. 12(e), P3 coating has incompletely destroyed films with many cracks and pitting. The elemental analysis of the two points A and B, (results shown in Table 5) shows a high concentration of oxygen, indicating that the dark films are passive film. Fig. 12(f) shows the morphology of the furrows in P3

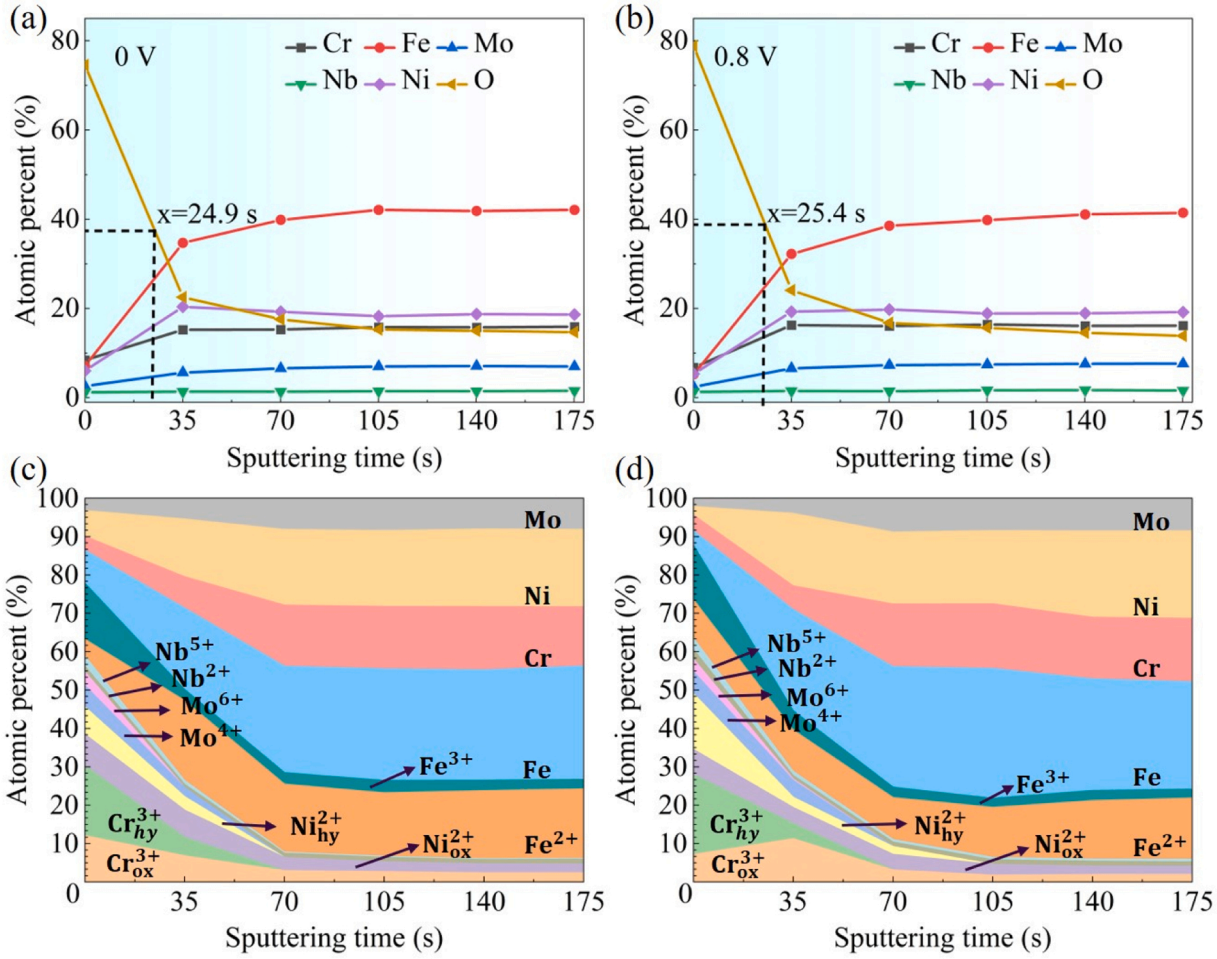

Fig. 10. XPS depth profiles of the passive films formed on the P3 coating in 3.5 wt% NaCl at different polarisation potentials: (a) 0 $V_{Ag/AgCl}$; (b) 0.8 $V_{Ag/AgCl}$; (c) and (d) are the derived chemical species of the elements.

coating. It can be seen that the abrasive wear of P3 is very weak, which is related to its higher corrosion resistance and hardness. The wear mechanisms of P3 coating and 304 SS in corrosion-wear are mainly abrasive wear, fatigue wear, and corrosive wear. Due to the brittle nature of the passive films, it tends to break up into small particles under cyclic loading and becomes a source of abrasive particles. On the other hand, the process of rupture-growth of the passive films, which is repeated over and over again, is also a major part of the material loss.

In order to further investigate the corrosion-wear behavior of the P3 coating in 3.5 wt% NaCl solution, the corrosion current density and friction coefficient were tested at different applying potentials of −0.5, −0.25, 0, 0.25, 0.35, and 0.5 $V_{Ag/AgCl}$, as shown in Fig. 13. As shown in Fig. 13(a), before sliding, the current densities at all applied potentials are negative due to the dominance of the cathodic reduction reaction of dissolved oxygen, indicating a state of cathodic polarisation and no corrosion. For −0.5 $V_{Ag/AgCl}$, the cathodic current increases during sliding due to the accelerated mass migration by the agitation of the solution and the fresh surfaces in the solution that promote the adsorption of oxygen, thus increasing the rate of oxygen reduction [46]. After sliding, the current returned to the initial level due to the restoration of mass migration conditions associated with the cathodic reaction [46]. For −0.25 and 0 $V_{Ag/AgCl}$, during sliding the measured current density increases slightly due to depassivation within the wear track but remains less than 0. Once sliding stops, the current density at both pressures decreases immediately and finally drops to the initial level. For 0.25, 0.35, and 0.5 $V_{Ag/AgCl}$, the current density increases dramatically as soon as sliding begins and continues to increase as sliding progresses. When sliding stops, the current drops quickly to the initial value. The corrosion current increases significantly with increasing applied potential, indicating that there is a significant wear-accelerated corrosion phenomenon during corrosion-wear, especially at the anodic potential. It can be seen from Fig. 13(b) that for −0.5 $V_{Ag/AgCl}$ and −0.25 $V_{Ag/AgCl}$, the friction coefficient is higher because no passive films is generated at the cathodic polarisation stage. The large fluctuations in the friction coefficient of 0 $V_{Ag/AgCl}$ are caused by discontinuous and incomplete passive films. The reason is that at 0 V, which is the critical state for passive films generation, the interference of wear produces discontinuous and incomplete passive films, and at the same time leads to the rupture of the passive films. The friction coefficients of 0.25, 0.35, and 0.5 $V_{Ag/AgCl}$ are drastically reduced due to the production of a stable passive films. In general, the friction coefficient decreases with increasing potential.

Fig. 13(c) shows the wear volume and wear rate at different applied potentials during corrosion-wear test. As the potential increases, the wear volume and wear rate also increase, with a slight increase when the applied potential is less than 0 $V_{Ag/AgCl}$ and a significant increase when the applied potential is greater than 0 $V_{Ag/AgCl}$. The volume loss at −0.5 $V_{Ag/AgCl}$ is considered to be pure wear, since the corrosion is negligible at −0.5 $V_{Ag/AgCl}$. For −0.25 $V_{Ag/AgCl}$ and 0 $V_{Ag/AgCl}$, there is only a slight increase in wear volume and wear rate, which is because it is still in the cathodic polarisation state, and corrosion and wear do not interact strongly. In the anodic polarization state, the wear volume and wear rate increase significantly with increasing applied potential. This is because as the applied potential increases, the synergistic effect of wear

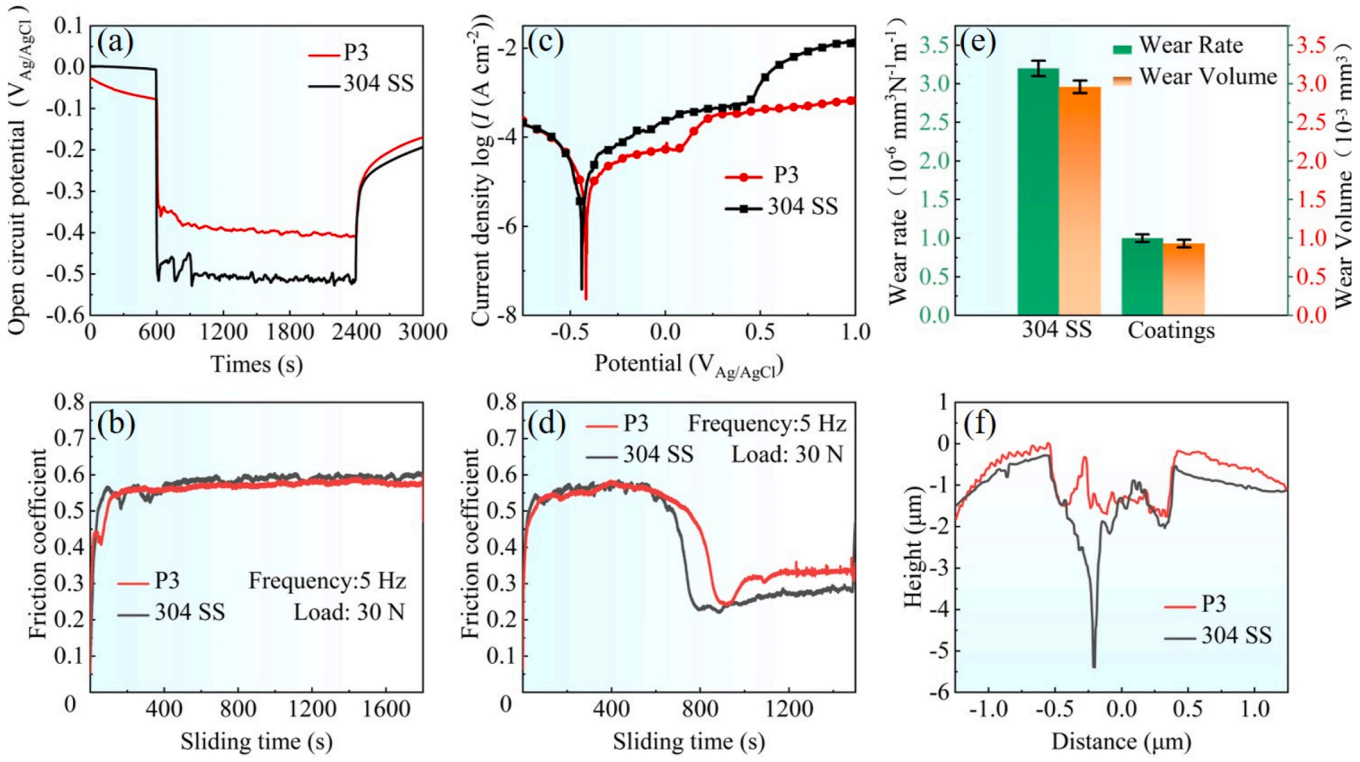

Fig. 11. (a) OCP, (b) friction coefficient under OCP; (c) potentiodynamic polarization curves, (d) friction coefficient under potentiodynamic polarization; (e) wear rate and wear volume, (f) surface profiles obtained for P3 coating and 304 SS under corrosion-wear condition in 3.5 wt% NaCl solution.

Table 4
Electrochemical parameters obtained from potentiodynamic polarization tests in Fig. 11(c).

Samples	P3	304 SS
E_{corr} (mV)	-404	-417
I_{corr} (μA cm^{-2})	34	43.7
$I_{pass(0.2\ V)}$ (μA cm^{-2})	195	420

and corrosion increases, leading to increased material loss. The corresponding wear tracks produced at different applied potentials are shown in Fig. 13(d). Apparently, the size of profiles increased with increasing applied potential. The material volume loss is very little and the contour size is small at applied potentials less than 0 $V_{Ag/AgCl}$. However, when the applied potential is greater than 0 $V_{Ag/AgCl}$, the contour size increases significantly with increasing applied potential, and the ridges appear at all wear edges, due to the pile-up of material resulting from the

Table 5
Element concentrations of Point A and Point B marked in Fig. 12(e).

Elements	O	Ni	Fe	Cr	Mo	Nb	total
A	61.22	19.78	10.48	6.44	1.91	0.17	100
B	31.18	17.51	26.07	20.46	3.95	0.82	100

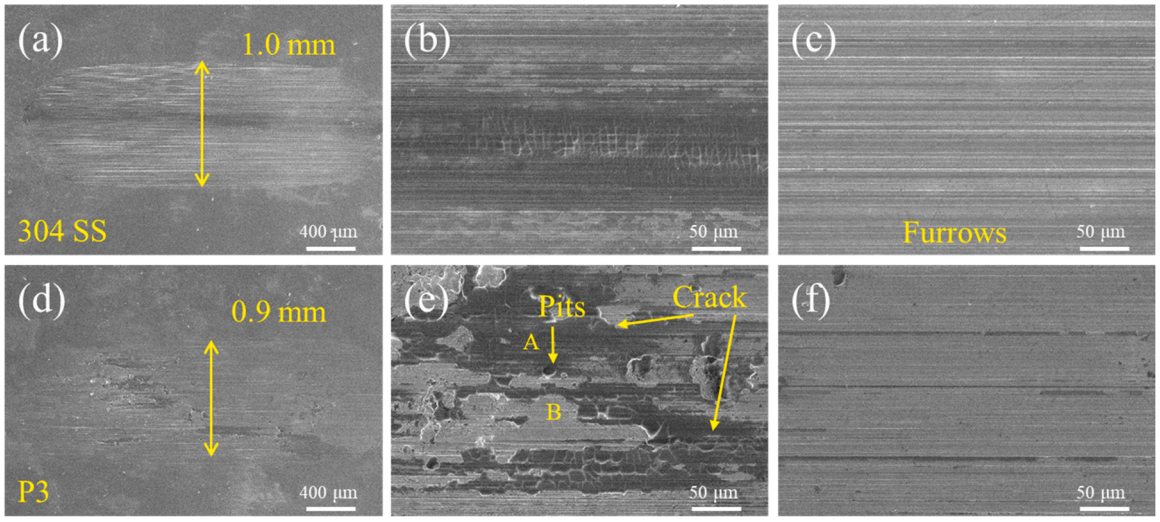

Fig. 12. SEM morphologies of the worn surfaces after corrosion-wear tests in 3.5 % NaCl solution. (a) 304 SS and (b, c) the enlarged images; (d) P3 coating and (e, f) the enlarged images.

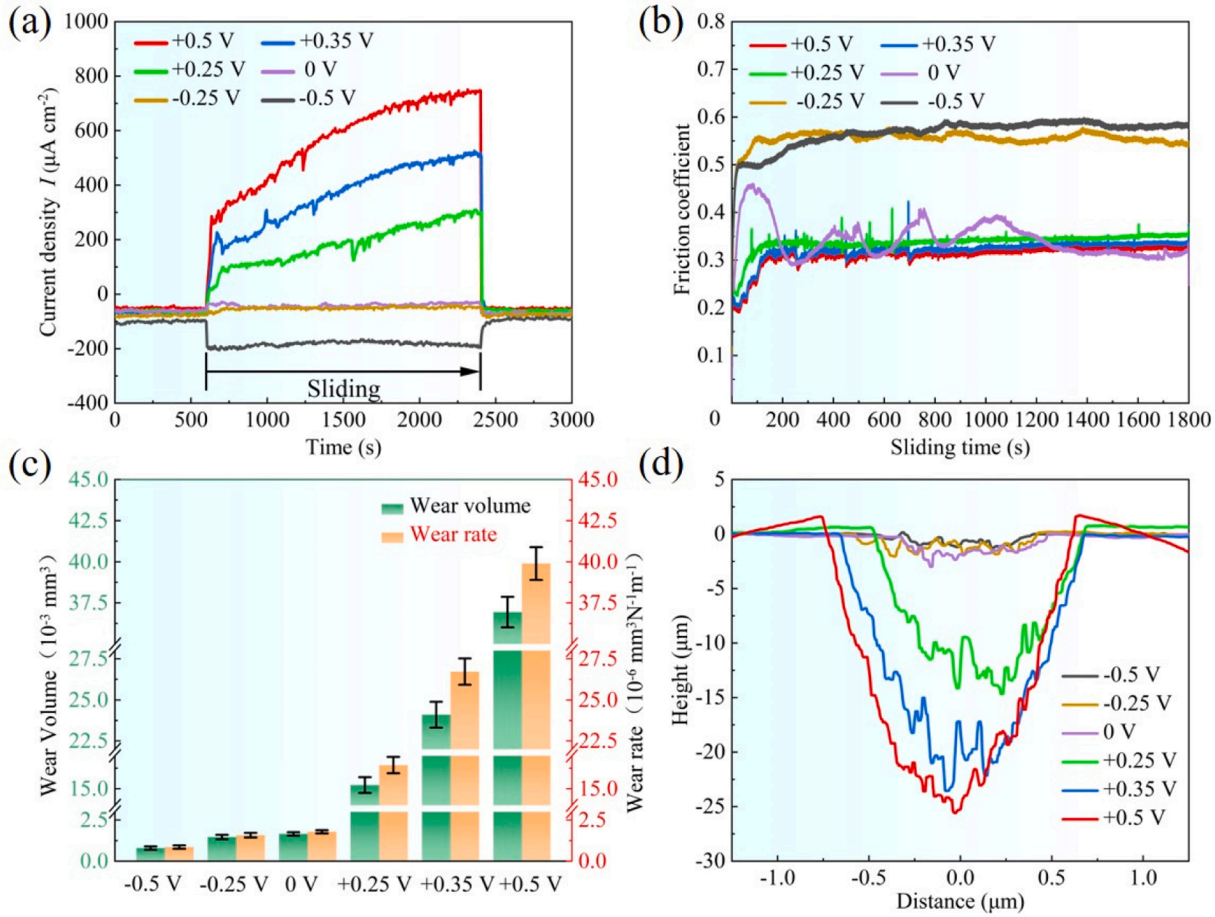

Fig. 13. (a) Evolution of the current, (b) friction coefficient, (c) wear rate and wear volume and (d) surface profiles for the P3 coating at different applied potentials in 3.5 wt% NaCl solution.

large plastic deformation produced during corrosion-wear. The change in wear profile is consistent with the analysis in Fig. 13(c).

Fig. 14 shows the wear tracks of P3 coating after under corrosion-wear tests in 3.5 wt% NaCl solution at different applied potentials. It can be seen that the P3 coating exhibits different failure mechanisms at different electrochemical states. In general, the size of the worn area increases with increasing applied potential, which is consistent with Fig. 13(d). As shown in Fig. 14(a, a_1), at −0.5 $V_{Ag/AgCl}$, the wear surface is characterized mainly by cracks in the deformed region leading to material fragmentation. The effect of corrosion is negligible and mechanical wear dominates. At −0.25 $V_{Ag/AgCl}$, the deformation area in the wear region is reduced and slight furrows appear. Applied anodic potential can obviously affect the wear mechanism and surface morphologies. When the applied potential is 0 $V_{Ag/AgCl}$, the whole wear area starts to show furrows, but the size and depth of the furrows are small. When the applied potential is higher than 0 $V_{Ag/AgCl}$, the whole wear area shows elongated scratches, i.e. furrows from abrasive wear, and some corrosion pits. As the applied potential increases pitting and furrows damage becomes more severe. Under the applied potential of OCP, the volume loss is mainly caused by mechanical wear, the wear mode is dominated by fatigue wear, and the loss due to corrosion is negligible. At applied potentials above the OCP, the volume loss is mainly due to a combination of abrasive wear, corrosive wear, and fatigue wear. The abrasive particles originate from the fragmentation of the passive films. It is possible to predict the failure mechanism of passive films at anodic potentials. The deterioration process can be divided into three steps: 1) The passive films formed on the wear surface is split into many large fragments, forming large cracks in the passive films; 2) Micro-cracks are formed within the fragments and split into smaller parts, leading to localized fragmentation due to uneven contact stress distribution; 3) Micro-fragments are removed due to friction and seawater impacts and then a new passive films is formed [81–83]. Successive removal-repair processes of passive films can generate significant amounts of corrosion, leading to significant wear-induced corrosion. At high potentials, the form-fragment-removal-repair of passive films is dominant and becomes an important part of the deterioration mechanism. On the other hand, the fragmentation of the passive films produced by corrosion promotes wear. The rapid repair of the passive films further accelerates the mechanical failure, resulting in corrosion-induced wear. In addition, rupture and detachment of the passive films reduces the actual contact area for subsequent cycles, leading to increased contact stresses and consequently higher wear rate.

Fig. 15(a) illustrates the effect of corrosion-wear synergy and the percentage of V_{WC} and V_{CW} to total material loss (V). As the applied potential increases, the corrosion-wear synergism is increasing. With the applied potential below OCP, the corrosion-wear synergy accounted for less than half of the total volume loss as it was still in the state of cathodic protection, and V_{CW} was negligible and V_{WC} represented the synergy. When the applied potential is higher than OCP, the corrosion-wear synergy increases dramatically, accounting for more than 90 % of the total volume loss. Among them, the proportion of V_{CW} gradually increases and the proportion of V_{WC} gradually decreases, which is because wear promotes corrosion more strongly. To further investigate the corrosion-wear synergy, Fig. 15(b) demonstrates the increase in corrosion current density, V_W, and V_C with increasing applied potential. At −0.5 V, the increase in corrosion current density is negative, and the cathodic polarisation state is strengthened, which is still a pure wear state. At −0.25 and 0 V, although the corrosion current density

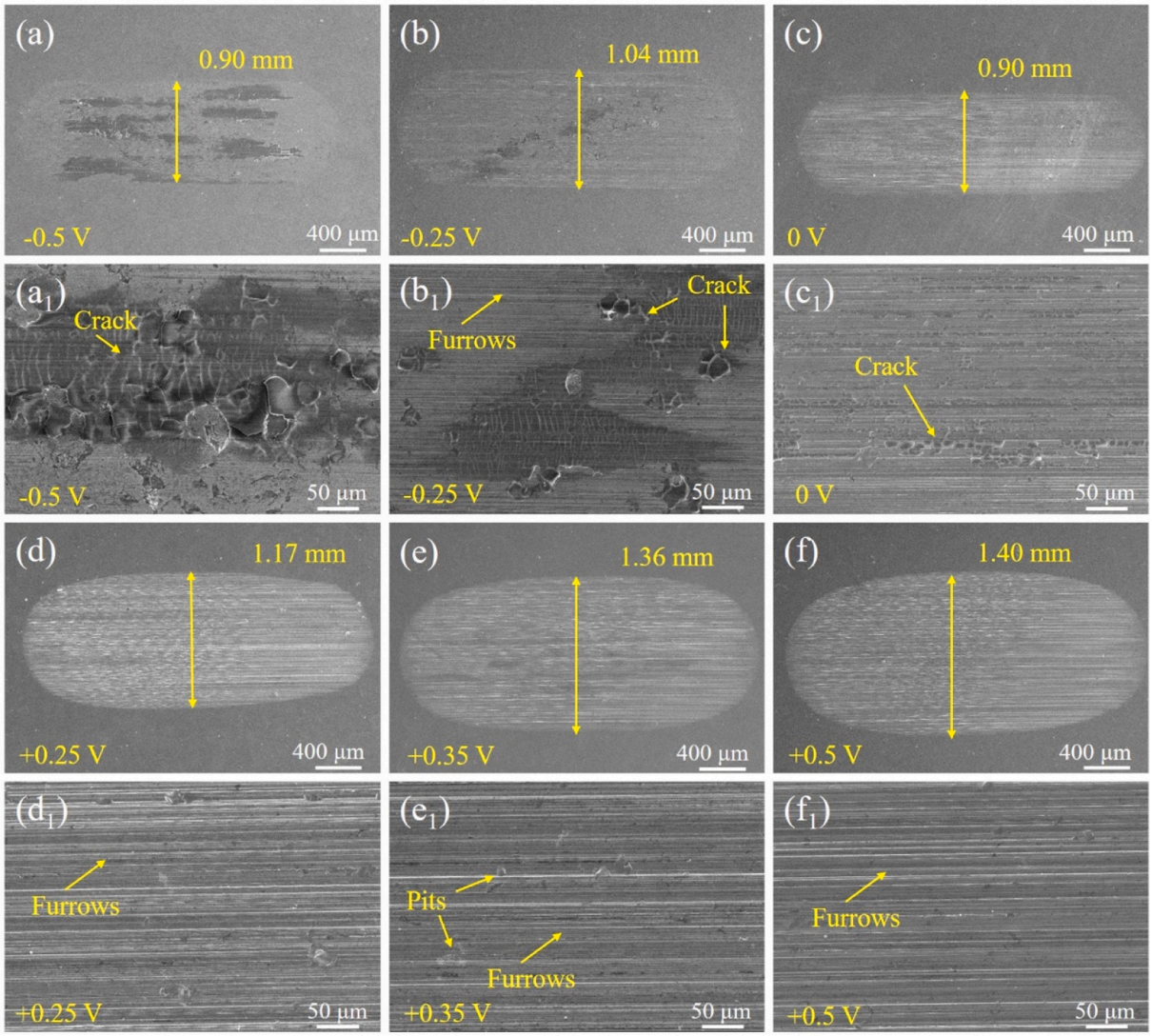

Fig. 14. The surface morphologies of wear track of P3 coating in 3.5 wt% NaCl solution at different potentials: (a) and (a_1) −0.5 $V_{Ag/AgCl}$; (b) and (b_1) −0.25 $V_{Ag/AgCl}$; (c) and (c_1) 0 $V_{Ag/AgCl}$; (d) and (d_1) 0.25 $V_{Ag/AgCl}$; (e) and (e_1) 0.35 $V_{Ag/AgCl}$; (f) and (f_1) 0.5 $V_{Ag/AgCl}$.

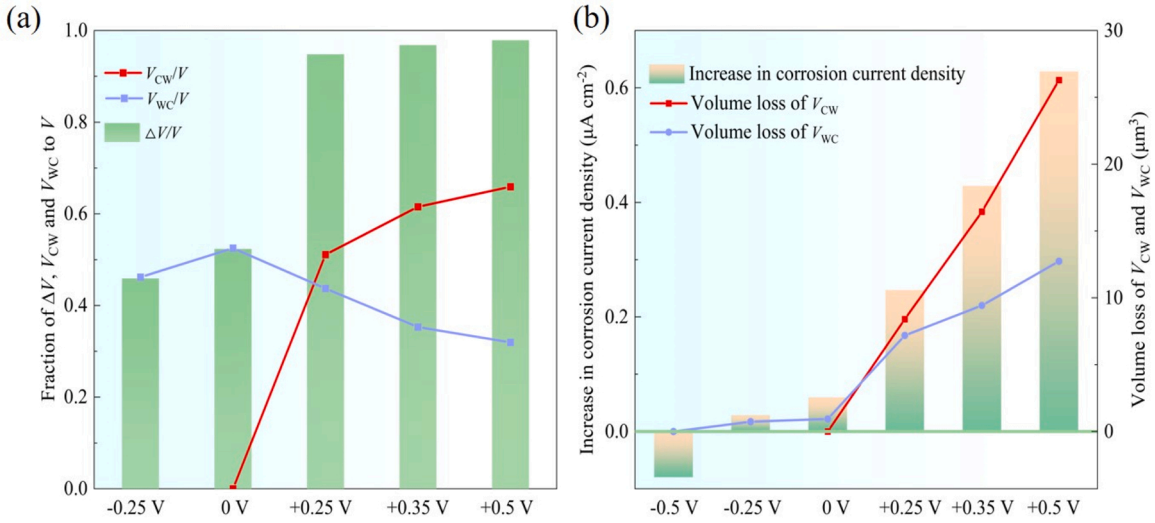

Fig. 15. (a) Fraction of ΔV, V_{CW} and V_{WC} to V; (b) increase in corrosion current density, volume loss of V_{CW} and V_{WC}.

increases, it is still in cathodic protection, and V_C can be neglected, then $\Delta V = V_W$. Below the OCP, the volume loss from corrosion-wear is small, due to the excellent corrosion-wear resistance of the coating and the lubricating effect of the solution. When the applied potential is higher than the OCP, the corrosion current density increases sharply with increasing potential, showing an approximately linear increase. This reflects a strong corrosion-wear interaction where wear promotes corrosion. Correspondingly, V_C also increases sharply with the increase of applied potential, showing an approximately linear growth relationship. V_W increases with increasing potential, but the increasing rate is much lower than that of V_C. This reflects a much stronger corrosion-promoting effect of wear. In combination with the previous analysis, the promotion of corrosion by wear is that the passive films ruptures under the action of wear, and the passive films goes through the the formation-breakage-formation process repeatedly, leading to the loss of material. Especially at high potentials, the increase in corrosion current makes the production of passive films more rapid, which accelerates this process and the material loss from corrosion. The promotion of wear by corrosion is that the rupture of the passive films occurs under cyclic loading due to its brittleness, and the ruptured passive films produces many small particles, which become a source of abrasive particles, leading to abrasive wear. It is clear that the interaction between corrosion and wear increases as the potential increases and is a mutually reinforcing relationship.

4. Conclusions

In this work, $Fe_{34}Ni_{20}Cr_{20}Mo_5B_4C_4P_{12}Nb_1$ (at %) high-entropy amorphous coatings were prepared by HVAF, and the effects of heat input on the microstructure and corrosion performance of the coating was investigated.

The P3 coating with the smallest heat input possesses low porosity (0.17 %), high amorphous content (82 %), and excellent corrosion resistance (8.2×10^{-7} A/ cm^2). The P3 coating has a very high passivation capacity with dense passive films, which can be attributed to the homogeneous structure and the high amorphous content. It was found that at higher heat input, small-sized powders tend to oxidize and form porous micro-oxidized zone, affecting the coating structure and corrosion resistance. Under the corrosion-wear conditions, the corrosion performance of the coating is better than that of 304 SS, and the volume loss is 1/3 of it. With the increase of the applied potential, the current density of the corrosion-wear process increases, and the synergism of corrosion and wear increases. When the applied potential is less than OCP, the corrosion process is suppressed and the volume loss of the coating is dominated by wear. When the applied potential is higher than the OCP, the volume loss from corrosion dominates. The $Fe_{34}Ni_{20}Cr_{20}Mo_5B_4C_4P_{12}Nb_1$ Fe-based amorphous coatings prepared by HVAF have excellent corrosion resistance and corrosion-wear performance as well as the advantage of low cost, which show a broad application prospect in the marine environment.

CRediT authorship contribution statement

Qianqian Wang: Writing – review & editing, Supervision, Project administration, Funding acquisition, Conceptualization. **Zhenjie Zhou:** Methodology, Investigation. **Baosen Zhang:** Resources, Conceptualization. **Yangzi Ye:** Writing – original draft, Methodology, Investigation, Data curation, Conceptualization. **Zhijun Guo:** Investigation, Conceptualization. **Baolong Shen:** Supervision, Project administration, Funding acquisition, Conceptualization.

Declaration of Competing Interest

The authors declare that they have no known competing financial interests or personal relationships that could have appeared to influence the work reported in this paper.

Data availability

Data will be made available on request.

Acknowledgments

This work was supported by Jiangsu Provincial Key R&D Program (BE2021088), National Natural Science Foundation of China (52231005), Opening Project of Jiangsu Key Laboratory of Advanced Structural Materials and Application Technology (ASMA202302), and Fundamental Research Funds for the Central Universities (2242023K40029).

References

[1] A. Inoue, A. Takeuchi, Recent development and application products of bulk glassy alloys, Acta Mater. 59 (2011) 2243–2267, https://doi.org/10.1016/j.actamat.2010.11.027.
[2] S.K. Nayak, A. Kumar, T. Laha, Fe-based metallic glass coatings by thermal spraying: a focused review on corrosion properties and related degradation mechanisms, Int. Mater. Rev. 68 (2023) 404–485, https://doi.org/10.1080/09506608.2022.2084670.
[3] H.X. Li, Z.C. Lu, S.L. Wang, Y. Wu, Z.P. Lu, Fe-based bulk metallic glasses: glass formation, fabrication, properties and applications, Prog. Mater. Sci. 103 (2019) 235–318, https://doi.org/10.1016/j.pmatsci.2019.01.003.
[4] W. Wang, C. Zhang, Z.W. Zhang, Y.C. Li, M. Yasir, H.T. Wang, L. Liu, Toughening Fe-based amorphous coatings by reinforcement of amorphous carbon, Sci. Rep. 7 (2017) 4084, https://doi.org/10.1038/s41598-017-04504-z.
[5] F.C. Li, T. Liu, J.Y. Zhang, S. Shuang, Q. Wang, A.D. Wang, J.G. Wang, Y. Yang, Amorphous–nanocrystalline alloys: fabrication, properties, and applications, Mater. Today Adv. 4 (2019) 100027, https://doi.org/10.1016/j.mtadv.2019.100027.
[6] R.Q. Guo, C. Zhang, Q. Chen, Y. Yang, N. Li, L. Liu, Study of structure and corrosion resistance of Fe-based amorphous coatings prepared by HVAF and HVOF, Corros. Sci. 53 (2011) 2351–2356, https://doi.org/10.1016/j.corsci.2010.12.022.
[7] Y. Wang, Y.G. Zheng, W. Ke, W.H. Sun, W.L. Hou, X.C. Chang, J.Q. Wang, Slurry erosion–corrosion behaviour of high-velocity oxy-fuel (HVOF) sprayed Fe-based amorphous metallic coatings for marine pump in sand-containing NaCl solutions, Corros. Sci. 53 (2011) 3177–3185, https://doi.org/10.1016/j.corsci.2011.05.062.
[8] E. Sadeghimeresht, N. Markocsan, P. Nylén, Microstructural characteristics and corrosion behavior of HVAF- and HVOF-sprayed Fe-based coatings, Surf. Coat. Technol. 318 (2017) 365–373, https://doi.org/10.1016/j.surfcoat.2016.11.088.
[9] B. Zhang, J. Cheng, X. Liang, Effects of Cr and Mo additions on formation and mechanical properties of Arc-sprayed FeBSiNb-based glassy coatings, J. Non-Cryst. Solids 499 (2018) 245–251, https://doi.org/10.1016/j.jnoncrysol.2018.07.035.
[10] D. Kong, C. Dong, X. Ni, L. Zhang, J. Yao, C. Man, X. Cheng, K. Xiao, X. Li, Mechanical properties and corrosion behavior of selective laser melted 316L stainless steel after different heat treatment processes, J. Mater. Sci. Technol. 35 (2019) 1499–1507, https://doi.org/10.1016/j.jmst.2019.03.003.
[11] A. Kumar, S.K. Nayak, P. Bijalwan, M. Dutta, A. Banerjee, T. Laha, Optimization of mechanical and corrosion properties of plasma sprayed low-chromium containing Fe-based amorphous/nanocrystalline composite coating, Surf. Coat. Technol. 370 (2019) 255–268, https://doi.org/10.1016/j.surfcoat.2019.05.010.
[12] Y. Fu, C. Huang, C. Du, J. Li, C. Dai, H. Luo, Z. Liu, X. Li, Evolution in microstructure, wear, corrosion, and tribocorrosion behavior of Mo-containing high-entropy alloy coatings fabricated by laser cladding, Corros. Sci. 191 (2021) 109727, https://doi.org/10.1016/j.corsci.2021.109727.
[13] H. Guo, S. Zhang, W. Sun, J. Wang, Differences in dry sliding wear behavior between HVAF-sprayed amorphous steel and crystalline stainless steel coatings, J. Mater. Sci. Technol. 35 (2019) 865–874, https://doi.org/10.1016/j.jmst.2018.11.006.
[14] C.A.C. Souza, D.V. Ribeiro, C.S. Kiminami, Corrosion resistance of Fe-Cr-based amorphous alloys: an overview, J. Non-Cryst. Solids 442 (2016) 56–66, https://doi.org/10.1016/j.jnoncrysol.2016.04.009.
[15] J.W. Li, L.J. Yang, H.R. Ma, K.M. Jiang, C.T. Chang, J.Q. Wang, Z.L. Song, X. M. Wang, R.W. Li, Improved corrosion resistance of novel Fe-based amorphous alloys, Mater. Des. 95 (2016) 225–230, https://doi.org/10.1016/j.matdes.2016.01.100.
[16] D.D. Xu, B.L. Zhou, Q.Q. Wang, J. Zhou, W.M. Yang, C.C. Yuan, L. Xue, X.D. Fan, L. Q. Ma, B.L. Shen, Effects of Cr addition on thermal stability, soft magnetic properties and corrosion resistance of FeSiB amorphous alloys, Corros. Sci. 138 (2018) 20–27, https://doi.org/10.1016/j.corsci.2018.04.006.
[17] J.E. Berger, A.M. Jorge, G.Y. Koga, V. Roche, C.S. Kiminami, C. Bolfarini, W. J. Botta, Influence of chromium concentration and partial crystallization on the corrosion resistance of FeCrNiB amorphous alloys, Mater. Charact. 179 (2021) 111369, https://doi.org/10.1016/j.matchar.2021.111369.
[18] M. Shi, S. Pang, T. Zhang, Towards improved integrated properties in FeCrPCB bulk metallic glasses by Cr addition, Intermetallics 61 (2015) 16–20, https://doi.org/10.1016/j.intermet.2015.02.010.
[19] X. Li, C. Qin, H. Kato, A. Makino, A. Inoue, Mo microalloying effect on the glass-forming ability, magnetic, mechanical and corrosion properties of

($Fe_{0.76}Si_{0.096}B_{0.084}P_{0.06}$)100-$_x$$Mo_x$ bulk glassy alloys, J. Alloy. Compd. 509 (2011) 7688–7691, https://doi.org/10.1016/j.jallcom.2011.04.081.
[20] P. Marcus, On some fundamental factors in the effect of alloying elements on passivation of alloys, Corros. Sci. 36 (1994) 2155–2158, https://doi.org/10.1016/0010-938X(94)90013-2.
[21] S.J. Pang, T. Zhang, K. Asami, A. Inoue, Formation of bulk glassy $Fe_{75-x-y}Cr_xMo_yC_{15}B_{10}$ alloys and their corrosion behavior, J. Mater. Res. 17 (2002) 701–704, https://doi.org/10.1557/JMR.2002.0100.
[22] Z.L. Long, C.T. Chang, Y.H. Ding, Y. Shao, P. Zhang, B.L. Shen, A. Inoue, Corrosion behavior of Fe-based ferromagnetic (Fe, Ni)–B–Si–Nb bulk glassy alloys in aqueous electrolytes, J. Non-Cryst. Solids 354 (2008) 4609–4613, https://doi.org/10.1016/j.jnoncrysol.2008.06.009.
[23] X.H. Ma, L. Zhang, X.H. Yang, Q. Li, Y.D. Huang, Effect of Ni addition on corrosion resistance of FePC bulk glassy alloy, Corros. Eng. Sci. Technol. 50 (2014) 433–437, https://doi.org/10.1179/1743278214y.0000000242.
[24] F. Zhai, E. Pineda, M.J. Duarte, D. Crespo, Role of Nb in glass formation of Fe–Cr–Mo–C–B–Nb BMGs, J. Alloy. Compd. 604 (2014) 157–163, https://doi.org/10.1016/j.jallcom.2014.03.095.
[25] S.D. Zhang, W.L. Zhang, S.G. Wang, X.J. Gu, J.Q. Wang, Characterisation of three-dimensional porosity in an Fe-based amorphous coating and its correlation with corrosion behaviour, Corros. Sci. 93 (2015) 211–221, https://doi.org/10.1016/j.corsci.2015.01.022.
[26] Y. Wang, S.L. Jiang, Y.G. Zheng, W. Ke, W.H. Sun, J.Q. Wang, Effect of porosity sealing treatments on the corrosion resistance of high-velocity oxy-fuel (HVOF)-sprayed Fe-based amorphous metallic coatings, Surf. Coat. Technol. 206 (2011) 1307–1318, https://doi.org/10.1016/j.surfcoat.2011.08.045.
[27] S.D. Zhang, J. Wu, W.B. Qi, J.Q. Wang, Effect of porosity defects on the long-term corrosion behaviour of Fe-based amorphous alloy coated mild steel, Corros. Sci. 110 (2016) 57–70, https://doi.org/10.1016/j.corsci.2016.04.021.
[28] J. Wu, S.D. Zhang, W.H. Sun, Y. Gao, J.Q. Wang, Enhanced corrosion resistance in Fe-based amorphous coatings through eliminating Cr-depleted zones, Corros. Sci. 136 (2018) 161–173, https://doi.org/10.1016/j.corsci.2018.03.005.
[29] Z. Zhou, L. Wang, F.C. Wang, H.F. Zhang, Y.B. Liu, S.H. Xu, Formation and corrosion behavior of Fe-based amorphous metallic coatings by HVOF thermal spraying, Surf. Coat. Technol. 204 (2009) 563–570, https://doi.org/10.1016/j.surfcoat.2009.08.025.
[30] J. Wu, S.D. Zhang, W.H. Sun, J.Q. Wang, Influence of oxidation related structural defects on localized corrosion in HVAF-sprayed Fe-based metallic coatings, Surf. Coat. Technol. 335 (2018) 205–218, https://doi.org/10.1016/j.surfcoat.2017.12.038.
[31] Y. Wang, Z.Z. Xing, Q. Luo, A. Rahman, J. Jiao, S.J. Qu, Y.G. Zheng, J. Shen, Corrosion and erosion–corrosion behaviour of activated combustion high-velocity air fuel sprayed Fe-based amorphous coatings in chloride-containing solutions, Corros. Sci. 98 (2015) 339–353, https://doi.org/10.1016/j.corsci.2015.05.044.
[32] Y. Yang, C. Zhang, Y. Peng, Y. Yu, L. Liu, Effects of crystallization on the corrosion resistance of Fe-based amorphous coatings, Corros. Sci. 59 (2012) 10–19, https://doi.org/10.1016/j.corsci.2012.02.003.
[33] J. Cheng, Q. Zhang, Y. Feng, S. Zhao, X. Liang, Microstructure and sliding wear behaviors of Plasma-sprayed Fe-based amorphous coatings in 3.5 wt% NaCl solution, J. Therm. Spray. Technol. 28 (2019) 1049–1059, https://doi.org/10.1007/s11666-019-00866-0.
[34] X.S. Wei, J.L. Jin, Z.Z. Jiang, D.D. Liang, J. Shen, FeCrMoWCBY metallic glass with high corrosion resistance in molten lead–bismuth eutectic alloy, Corros. Sci. 190 (2021) 109688, https://doi.org/10.1016/j.corsci.2021.109688.
[35] D.B. Wang, J. Wu, J.P. Cui, Q. Wang, T.R. Li, W. Emori, S.D. Zhang, J.Q. Wang, Long-term corrosion evolution associated with the structural heterogeneities of an Fe-based amorphous coating in H_3BO_3 solution at various temperatures, J. Mater. Sci. Technol. 140 (2023) 233–248, https://doi.org/10.1016/j.jmst.2022.08.039.
[36] P. Pan, W. Zhou, Y. Zhao, Y. Wang, N. Zhang, Hot corrosion behavior of an arc sprayed Fe-based amorphous coating in a simulated biomass firing environment, Corros. Sci. 194 (2022) 109938, https://doi.org/10.1016/j.corsci.2021.109938.
[37] J. Wu, J.P. Cui, Q.J. Zheng, S.D. Zhang, W.H. Sun, B.J. Yang, J.Q. Wang, Insight into the corrosion evolution of Fe-based amorphous coatings under wet-dry cyclic conditions, Electrochim. Acta 319 (2019) 966–980, https://doi.org/10.1016/j.electacta.2019.07.058.
[38] A. Kumar, R. Kumar, P. Bijalwan, M. Dutta, A. Banerjee, T. Laha, Fe-based amorphous/nanocrystalline composite coating by plasma spraying: effect of heat input on morphology, phase evolution and mechanical properties, J. Alloy. Compd. 771 (2019) 827–837, https://doi.org/10.1016/j.jallcom.2018.09.024.
[39] A. Kumar, S.K. Nayak, K. Sarkar, A. Banerjee, K. Mondal, T. Laha, Investigation of nano- and micro-scale structural evolution and resulting corrosion resistance in plasma sprayed Fe-based (Fe-Cr-B-C-P) amorphous coatings, Surf. Coat. Technol. 397 (2020) 126058, https://doi.org/10.1016/j.surfcoat.2020.126058.
[40] B. Huang, C. Zhang, G. Zhang, H. Liao, Wear and corrosion resistant performance of thermal-sprayed Fe-based amorphous coatings: a review, Surf. Coat. Technol. 377 (2019) 124896, https://doi.org/10.1016/j.surfcoat.2019.124896.
[41] H.J. Farmer, J, Wong F, et al, Iron-Based Amorphous Metals: High-Performance Corrosion-Resistant Material Development, Metall. Mater.Trans. A Phys. Metall. Mater. Sci. 40A (2009) 1289-1305, https://doi.org/10.1007/s11661-008-9779-8.
[42] F. Shu, B. Zhang, T. Liu, S. Sui, Y. Liu, P. He, B. Liu, B. Xu, Effects of laser power on microstructure and properties of laser cladded CoCrBFeNiSi high-entropy alloy amorphous coatings, Surf. Coat. Technol. 358 (2019) 667–675, https://doi.org/10.1016/j.surfcoat.2018.10.086.
[43] J.B. Cheng, B. Sun, Y.Y. Ge, X.L. Hu, L.H. Zhang, X.B. Liang, X.C. Zhang, Effect of B/Si ratio on structure and properties of high-entropy glassy $Fe_{25}Co_{25}Ni_{25}(B_xSi_{1-x})_{25}$ coating prepared by laser cladding, Surf. Coat. Technol. 402 (2020) 126320, https://doi.org/10.1016/j.surfcoat.2020.126320.
[44] Y. Li, S. Wang, X. Wang, M. Yin, W. Zhang, New FeNiCrMo(P, C, B) high-entropy bulk metallic glasses with unusual thermal stability and corrosion resistance, J. Mater. Sci. Technol. 43 (2020) 32–39, https://doi.org/10.1016/j.jmst.2020.01.020.
[45] Z.J. Zhou, Design and Preparation of Iron-based Amorphous Coating and Investigation of Its Corrosion and Wear Resistance, Southeast university, 2022.
[46] P. Ren, H. Meng, Q. Xia, Z. Zhu, M. He, Tribocorrosion of 316L stainless steel by in-situ electrochemical methods under deep-sea high hydrostatic pressure environment, Corros. Sci. 202 (2022) 110315, https://doi.org/10.1016/j.corsci.2022.110315.
[47] J. Jiang, M.M. Stack, A. Neville, Modelling the tribo-corrosion interaction in aqueous sliding conditions, Tribol. Int. 35 (2002) 669–679, https://doi.org/10.1016/S0301-679X(02)00058-0.
[48] C.Y. Lee, W.T. Mao, M.D. Ger, H.B. Lee, A study on the corrosion and wear behavior of nanocrystalline Ni Mo electrodeposited coatings, Surf. Coat. Technol. 366 (2019) 286–295, https://doi.org/10.1016/j.surfcoat.2019.03.048.
[49] S.W. Watson, F.J. Friedersdorf, B.W. Madsen, S.D. Cramer, Methods of measuring wear-corrosion synergism, Wear 181 (1995) 476–484, https://doi.org/10.1016/0043-1648(95)90161-2.
[50] D. Zois, A. Lekatou, M. Vardavoulias, Preparation and characterization of highly amorphous HVOF stainless steel coatings, J. Alloy. Compd. 504 (2010) 283–287, https://doi.org/10.1016/j.jallcom.2010.02.062.
[51] H.R. Ma, X.Y. Chen, J.W. Li, C.T. Chang, G. Wang, H. Li, X.M. Wang, R.W. Li, Fe-based amorphous coating with high corrosion and wear resistance, Surf. Eng. 33 (2017) 56–62, https://doi.org/10.1080/02670844.2016.1176718.
[52] H.B. Lee, T.J. Lin, C.Y. Lee, Corrosion of high-velocity-oxygen-fuel (HVOF) sprayed non-crystalline alloy coating in marine environment, Surf. Coat. Technol. 409 (2021) 126896, https://doi.org/10.1016/j.surfcoat.2021.126896.
[53] Y.J. Sun, R. Yang, L. Xie, Y.B. Li, S.L. Wang, H.X. Li, W.R. Wang, J.S. Zhang, Interfacial bonding and corrosion behaviors of HVOF-sprayed Fe-based amorphous coating on 8090 Al-Li alloy, Surf. Coat. Technol. 436 (2022) 128316, https://doi.org/10.1016/j.surfcoat.2022.128316.
[54] G. Wang, Z. Huang, P. Xiao, X. Zhu, Spraying of Fe-based amorphous coating with high corrosion resistance by HVAF, J. Manuf. Process. 22 (2016) 34–38, https://doi.org/10.1016/j.jmapro.2016.01.009.
[55] H.R. Ma, J.W. Li, C.T. Chang, X.M. Wang, R.W. Li, Passivation Behavior of Fe-Based Amorphous Coatings Prepared by High-Velocity Air/Oxygen Fuel Processes, J. Therm. Spray. Technol. 26 (2017) 2040–2047, https://doi.org/10.1007/s11666-017-0647-1.
[56] X. Liu, Y. Wu, Z. Qiu, Z. Lu, S. Yao, S. Zhuo, D. Zeng, Simultaneously enhancing wear and corrosion resistance of HVAF-sprayed Fe-based amorphous coating from Mo clad feedstock, J. Mater. Process Technol. 302 (2022) 117465, https://doi.org/10.1016/j.jmatprotec.2021.117465.
[57] F. Huang, J.J. Kang, W. Yue, X.B. Liu, Z.Q. Fu, L.N. Zhu, D.S. She, G. Ma, H. D. Wang, J. Liang, W. Weng, C.B. Wang, Effect of heat treatment on erosion–corrosion of Fe-based amorphous alloy coating under slurry impingement, J. Alloy. Compd. 820 (2020) 153132, https://doi.org/10.1016/j.jallcom.2019.153132.
[58] R. Jindal, V.S. Raja, M.A. Gibson, M.J. Styles, T.J. Bastow, C.R. Hutchinson, Effect of annealing below the crystallization temperature on the corrosion behavior of Al–Ni–Y metallic glasses, Corros. Sci. 84 (2014) 54–65, https://doi.org/10.1016/j.corsci.2014.03.015.
[59] C. Liu, Q. Bi, A. Matthews, EIS comparison on corrosion performance of PVD TiN and CrN coated mild steel in 0.5 N NaCl aqueous solution, Corros. Sci. 43 (2001) 1953–1961, https://doi.org/10.1016/S0010-938X(00)00188-8.
[60] C. Liu, Q. Bi, A. Leyland, A. Matthews, An electrochemical impedance spectroscopy study of the corrosion behaviour of PVD coated steels in 0.5 N NaCl aqueous solution: Part I. Establishment of equivalent circuits for EIS data modelling, Corros. Sci. 45 (2003) 1243–1256, https://doi.org/10.1016/S0010-938X(02)00214-7.
[61] C. Liu, Q. Bi, A. Leyland, A. Matthews, An electrochemical impedance spectroscopy study of the corrosion behaviour of PVD coated steels in 0.5 N NaCl aqueous solutionPart II. EIS interpretation of corrosion behaviour, Corros. Sci. 45 (2003) 1257–1273, https://doi.org/10.1016/S0010-938X(02)00214-7.
[62] H.Z. Wang, Y.H. Cheng, J.Y. Yang, Q.Q. Wang, Influence of laser remelting on organization, mechanical properties and corrosion resistance of Fe-based amorphous composite coating, Surf. Coat. Technol. 414 (2021) 127081, https://doi.org/10.1016/j.surfcoat.2021.127081.
[63] M. Magnani, P.H. Suegama, N. Espallargas, S. Dosta, C.S. Fugivara, J. M. Guilemany, A.V. Benedetti, Influence of HVOF parameters on the corrosion and wear resistance of WC-Co coatings sprayed on AA7050 T7, Surf. Coat. Technol. 202 (2008) 4746–4757, https://doi.org/10.1016/j.surfcoat.2008.04.055.
[64] C.H. Hsu, F. Mansfeld, Technical note: concerning the conversion of the constant phase element parameter y0 into a capacitance, Corrosion 57 (2001) 747–748, https://doi.org/10.5006/1.3280607.
[65] Y.Y. Ge, J.B. Cheng, J.Y. Mo, L. Xue, B.S. Zhang, S. Hong, Y.P. Wu, X.B. Liang, X. C. Zhang, Experimental and DFT studies on corrosion behaviors of laser-cladded $(FeCoNi)_{75-x}Cr_xB_{15}Si_{10}$ high-entropy alloy coatings, J. Alloy. Compd. 976 (2024) 173173, https://doi.org/10.1016/j.jallcom.2023.173173.
[66] G. Meng, Y. Shao, T. Zhang, Y. Zhang, F. Wang, Synthesis and corrosion property of pure Ni with a high density of nanoscale twins, Electrochim. Acta 53 (2008) 5923–5926, https://doi.org/10.1016/j.electacta.2008.03.070.
[67] X. Yuan, Z.F. Yue, X. Chen, S.F. Wen, L. Li, T. Feng, EIS study of effective capacitance and water uptake behaviors of silicone-epoxy hybrid coatings on mild

steel, Prog. Org. Coat. 86 (2015) 41–48, https://doi.org/10.1016/j.porgcoat.2015.04.004.
[68] L. Aïnouche, L. Hamadou, A. Kadri, N. Benbrahim, D. Bradai, Interfacial barrier layer properties of three generations of TiO2 nanotube arrays, Electrochim. Acta 133 (2014) 597–609, https://doi.org/10.1016/j.electacta.2014.04.086.
[69] M.E.O.B. Hirschorn, B. Tribollet, V. Vivier, I. Frateur, M. Musianid, Constant-phase-element behavior caused by resistivity distributions in films II. Applications, J. Electrochem. Soc. 157 (2010) C458–C463, https://doi.org/10.1149/1.3499565.
[70] S.J. Pang, C.H. Shek, T. Zhang, K. Asami, A. Inoue, Corrosion behavior of glassy $Ni_{55}Co_5Nb_{20}Ti_{10}Zr_{10}$ alloy in 1N HCl solution studied by potentiostatic polarization and XPS, Corros. Sci. 48 (2006) 625–633, https://doi.org/10.1016/j.corsci.2005.02.013.
[71] M. Lohrengel, Thin anodic oxide layers on aluminium and other valve metals: high field regime, Mater. Sci. Eng. R: Rep. 11 (1993) 243–294, https://doi.org/10.1016/0927-796X(93)90005-N.
[72] J. Schultze, M. Lohrengel, D. Ross, Nucleation and growth of anodic oxide films, Electrochim. Acta 28 (1983) 973–984, https://doi.org/10.1016/0013-4686(83)85175-5.
[73] Z. Li, C. Zhang, L. Liu, Wear behavior and corrosion properties of Fe-based thin film metallic glasses, J. Alloy. Compd. 650 (2015) 127–135, https://doi.org/10.1016/j.jallcom.2015.07.256.
[74] H. Luo, C.F. Dong, K. Xiao, X.G. Li, Characterization of passive film on 2205 duplex stainless steel in sodium thiosulphate solution, Appl. Surf. Sci. 258 (2011) 631–639, https://doi.org/10.1016/j.apsusc.2011.06.077.
[75] J. Amri, T. Souier, B. Malki, B. Baroux, Effect of the final annealing of cold rolled stainless steels sheets on the electronic properties and pit nucleation resistance of passive films, Corros. Sci. 50 (2008) 431–435, https://doi.org/10.1016/j.corsci.2007.08.013.
[76] P. Qin, L.Y. Chen, C.H. Zhao, Y.J. Liu, C.D. Cao, H. Sun, L.C. Zhang, Corrosion behavior and mechanism of selective laser melted Ti35Nb alloy produced using pre-alloyed and mixed powder in Hank's solution, Corros. Sci. 189 (2021) 109609, https://doi.org/10.1016/j.corsci.2021.109609.
[77] L.Y. Chen, H.Y. Zhang, C.B. Zheng, H.Y. Yang, P. Qin, C.H. Zhao, S. Lu, S.X. Liang, L.J. Chai, L.C. Zhang, Corrosion behavior and characteristics of passive films of laser powder bed fusion produced Ti-6Al-4V in dynamic Hank's solution, Mater. Des. 208 (2021) 109907, https://doi.org/10.1016/j.matdes.2021.109907.
[78] N. Diomidis, J.P. Celis, P. Ponthiaux, F. Wenger, Tribocorrosion of stainless steel in sulfuric acid: Identification of corrosion–wear components and effect of contact area, Wear 269 (2010) 93–103, https://doi.org/10.1016/j.wear.2010.03.010.
[79] J.P. Celis, P. Ponthiaux, F. Wenger, Tribo-corrosion of materials: interplay between chemical, electrochemical, and mechanical reactivity of surfaces, Wear 261 (2006) 939–946, https://doi.org/10.1016/j.wear.2006.03.027.
[80] P. Ponthiaux, F. Wenger, D. Drees, J.P. Celis, Electrochemical techniques for studying tribocorrosion processes, Wear 256 (2004) 459–468, https://doi.org/10.1016/s0043-1648(03)00556-8.
[81] C.Y. Lee, T.J. Lin, H.H. Sheu, H.B. Lee, A study on corrosion and corrosion-wear behavior of Fe-based amorphous alloy coating prepared by high velocity oxygen fuel method, J. Mater. Res. Technol. 15 (2021) 4880–4895, https://doi.org/10.1016/j.jmrt.2021.10.103.
[82] Y. Zhu, M. Dong, J. Li, L. Wang, The improved corrosion and tribocorrosion properties of TiSiN/Ag by thermal treatment, Surf. Coat. Technol. 385 (2020) 125437, https://doi.org/10.1016/j.surfcoat.2020.125437.
[83] D. Landolt, S. Mischler, M. Stemp, Electrochemical methods in tribocorrosion: a critical appraisal, Electrochim. Acta 46 (2001) 3913–3929, https://doi.org/10.1016/S0013-4686(01)00679-X.